Which way is up?—experiences with processing physical modeling data

David C. Henley and Joe Wong

ABSTRACT

In the initial stages of an exploration project, a seismic data processor is often presented with a set of seismic data acquired over a geological prospect whose subsurface features and properties are either partially or completely unknown. It is then the processor's job to extract as much of this detail as possible through appropriate data processing. To simulate and illustrate the process, two data sets from the CREWES physical modeling facility were acquired by Wong (henceforth known as the Modeller) and presented to Henley (termed the Processor) for imaging, but *with no information conveyed about the physical model structure or materials*, except that the two surveys simulated 'baseline' and 'time-lapse' realizations of the *same* model. Each set of seismic data was processed independently, and algorithm parameters were deduced only from the data characteristics. Features of the processed data were then used to evaluate three different proposed 'models' supplied by the Modeller. Only one of these was consistent with images and other information obtained from the processed seismic data. This experiment was a very instructive illustration of the seismic exploration process.

The 'time-lapse' version of the model created a family of strong multiple reflections in the corresponding seismic data. As part of our analytic processing, we used this opportunity to test a multiple-elimination technique applied in the common-ray-parameter domain. Two variations of the technique were found effective on surface-related multiples in this geometrically simple model. We expect the same technique to be useful on seismic field data as well, but it probably loses its effectiveness with increasing geological complexity, decreasing regularity of acquisition geometry, and additive noise.

INTRODUCTION

Physical modeling is attractive not only because it allows us to study elastic wave propagation in a controlled environment, but because it allows us to test the effectiveness of our processing on seismic field data by analysing and imaging realistic data from the physical model measurements. The relatively simple geometry of many physical models, as well as the carefully controlled selection of materials leads to relatively easy identification of various wave modes. This, in turn, aids the construction of processing streams and their parameters, aimed at enhancing selected modes and either measuring their attributes to verify seismic theory, or using them to construct images.

Much of what we term exploration seismology is centred on recording and processing the reflections of outgoing seismic waves from rock layer boundaries in the earth, so that we can image the layer boundaries and potentially extract information about the lithology and fluid content of the layers. While the goal of much current research is to invert the complete backscattered wavefield, most practical efforts still focus on extracting and imaging a single mode, such as simple reflected (or converted) energy, while eliminating other modes like surface waves (outgoing and scattered), refractions, and multiply-

reflected waves. Hence, significant effort has been expended to develop wavefield separation techniques, including multiple-attenuation algorithms.

The two closely related physical models ('baseline' and 'time-lapse') used in this study were surveyed using identical acquisition parameters in the CREWES physical modeling facility (Wong, et al, 2010, 2011). In each case, the acquisition simulated a series of shots into a receiver line extending across the surface of the physical model, where the shot positions were offset slightly from the receiver line. For each survey, this created a series of what were, actually, 3D receiver-line trace gathers; but we processed each set of gathers as if it was a 2D line, since the source offset was the same for each gather.

At each stage of the processing, the data were visually examined for clues about the structure of the model. In what follows, we lead the reader through our analysis of the two physical models and their characteristics, as if they were new seismic prospects.

ANALYTIC PROCESSING

The two physical model data sets are called 'model B' and 'model E' to distinguish them, and we show equivalent stages in the processing of the two sets simultaneously, beginning with examination of the raw data in receiver-line gathers. We then proceed to wavefield separation, including coherent noise attenuation and multiple attenuation, then to CMP stacking. At each stage we summarize observations, and describe how the two data sets differ. We then consider, in turn, diagrams of three hypothetical physical models and eliminate two of them due to their incompatibility with processed seismic images.

Raw data observations

A receiver line gather from near the centre of model B is displayed in Figure 1, processed only with AGC to make smaller amplitude events more visible. Figure 2 shows the equivalent gather from model E. All times, distances, and velocities on these plots, and those which follow, are expressed in 'scaled' units, relating them directly to full field-scale seismic surveys. The most obvious feature on each of the Figures 1 and 2 is the presence of both direct-arrival events and ground-roll events. The former appear to have a linear moveout velocity of about 2400m/s, while the latter are less than half that value. Furthermore, the ground-roll is positively identified by its mild dispersion, which can be seen on both displays. Note, as well, that the ground roll appears to be regenerated by reflecting from various layer boundaries in the models, including what is possibly the bottom of the entire model at about 1.8s. The presence and strength of these coherent events, as well as the absence of ghosts on event waveforms, tell us that both models have a solid medium, rather than water, as the uppermost layer. If these strong linear events are left unattenuated, CMP stacking does not adequately cancel them, as shown for model E in Figure 3.

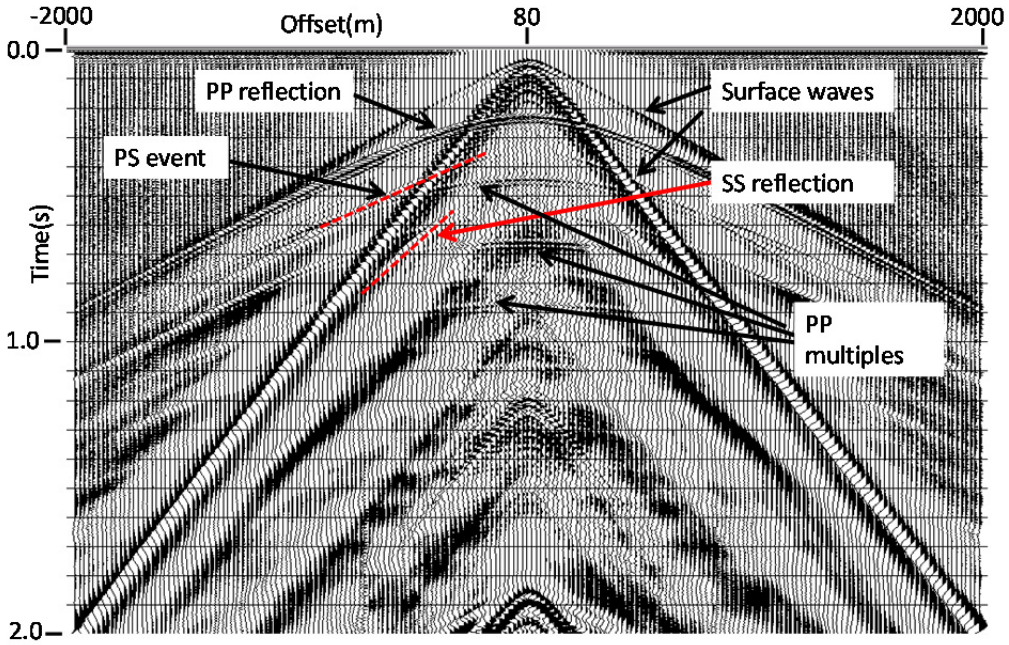

FIG. 1. Raw receiver line gather from Model B. AGC has been applied for display purposes. Various events have been tentatively identified.

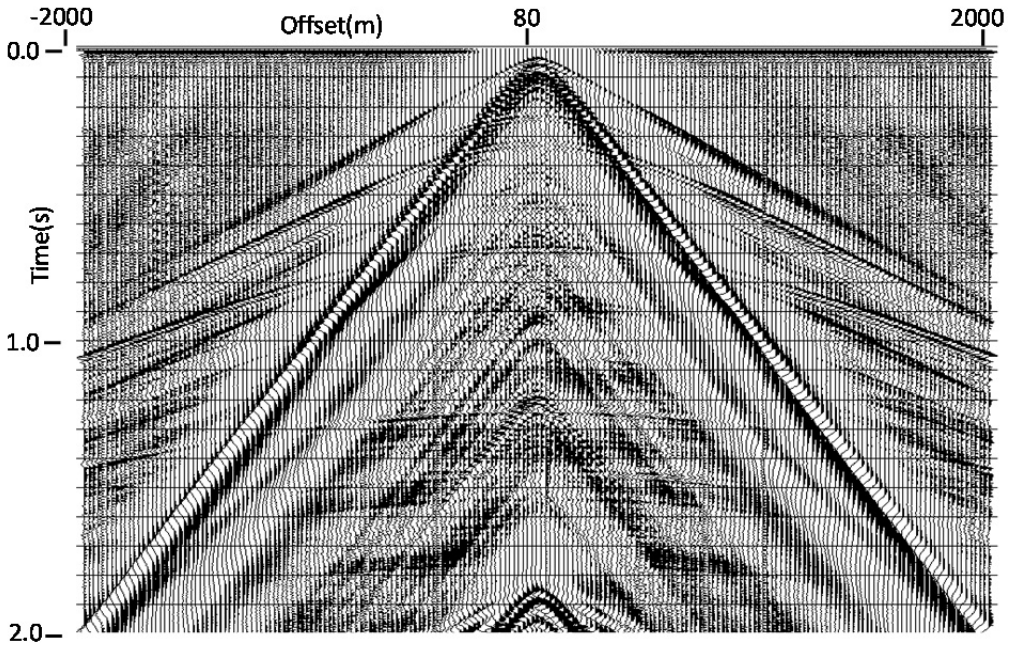

FIG. 2. Raw receiver line gather from Model E. AGC has been applied for display purposes. Deeper reflection events are more visible on this record than on the one in Figure 1.

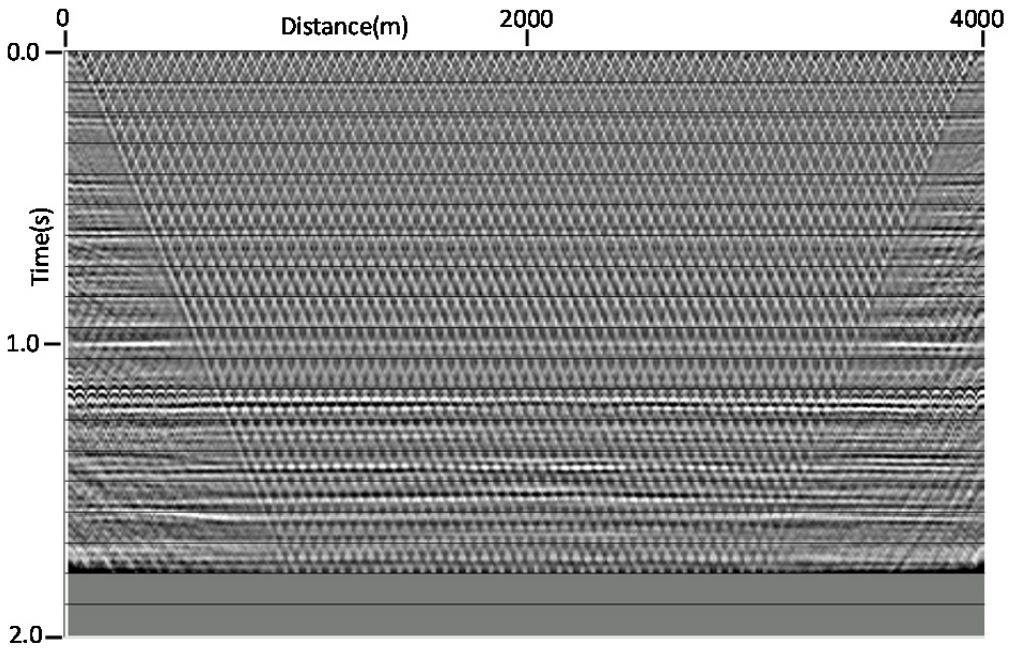

FIG. 3. CMP stack of the receiver line gathers for Model E. The surface waves are obviously inadequately attenuated and interfere greatly with reflections.

Coherent noise attenuation

We have found radial trace filtering techniques to be very effective for removing most types of coherent, source-generated noise; and we used them on these model data, as well (Henley, 2003, 2011). In addition to their effectiveness, the methods have the advantage of leaving reflection event amplitudes unaffected, since they subtract noise estimates whose frequency content in the radial trace domain is exclusive of that of the reflections. For these data sets, a series of three radial trace filters was designed. The first filter is a radial trace fan filter which estimates and subtracts all linear events passing through the apparent source origin of the trace gather (and the coincident origin of the RT fan); and the subsequent two filters are RT dip filters which estimate and subtract all linear events parallel to the primary ground roll event (such as regenerated ground roll).

Because a raw trace gather is generally a poorly conditioned matrix (values near the time and offset origin are many orders of magnitude larger than values at large time and offset), we applied AGC to the gather, with the option for later removal. We show in Figure 4 the raw trace gather from model B in Figure 1 after application of the AGC and RT filter series. The removal of the strong noise trains has left regions of weak amplitudes on the gather, so we removed the previously-applied AGC to restore the original amplitudes. Then we applied a second AGC to the de-noised data, resulting in the gather in Figure 5. Various hyperbolic events are now plainly visible on the gather, including what we interpret as PS and SS events. We then used a display option in ProMAX to fit hyperbolae to any visible coherent events in order to verify event identification and to estimate NMO velocity for CMP stacking of the PP events. Figure 6 shows the comparable trace gather from model E. Interestingly, while a possible SS event

and its multiple can be found, no PS event is evident, even though the gather is less noisy after the filtering operation than the gather for model B.

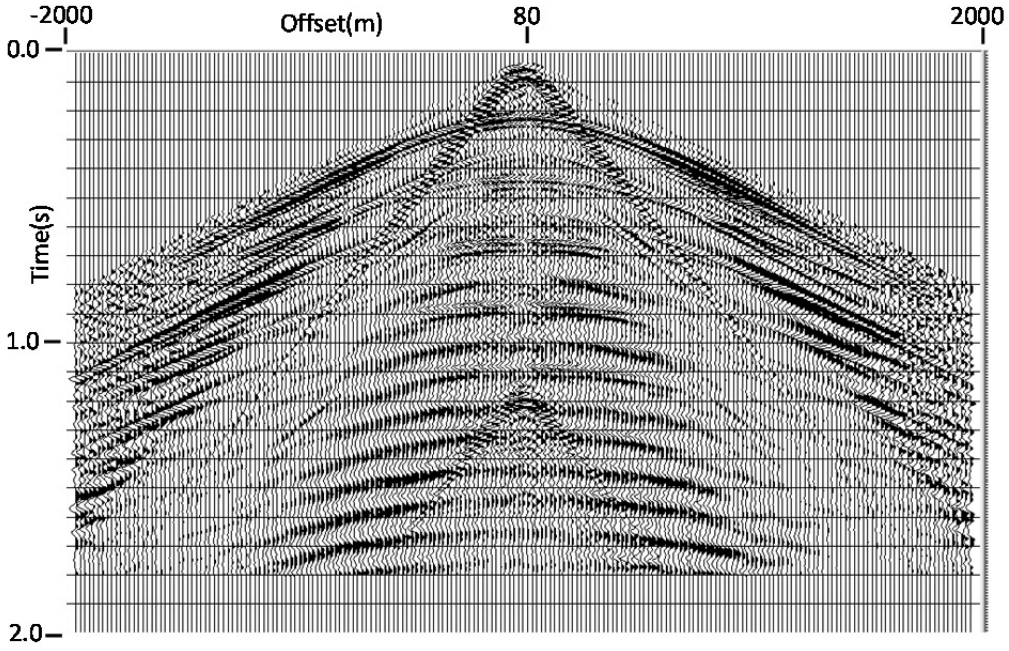

FIG. 4. Model B receiver line gather after AGC and RT filtering to remove surface wave noise.

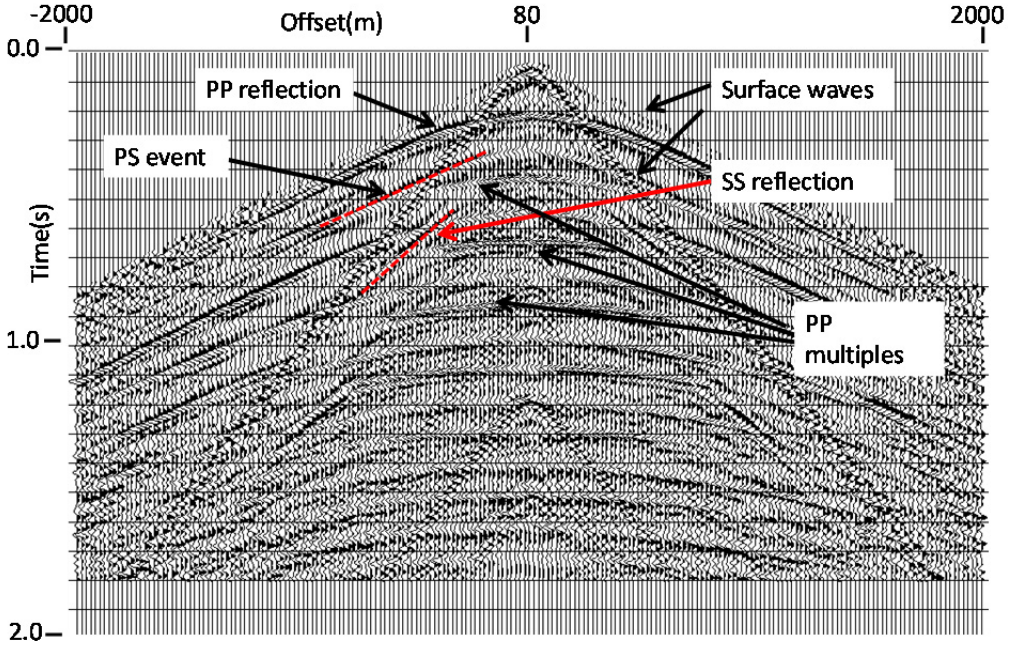

FIG. 5. Model B receiver line gather after AGC, RT filtering, AGC restoration and re-application.

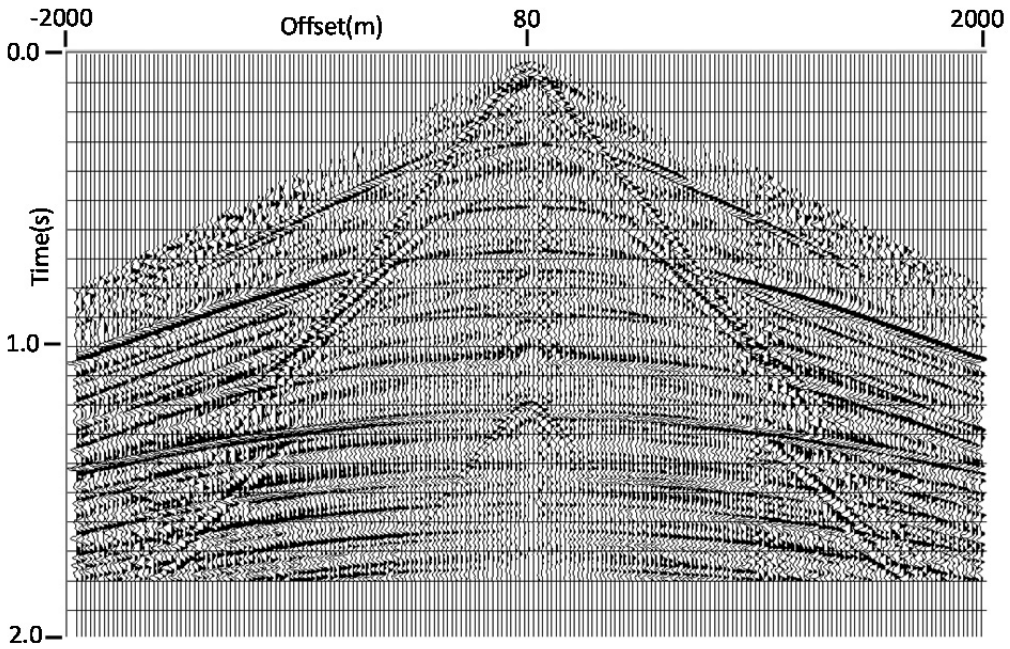

FIG. 6. Model E receiver line gather after AGC, RT filtering, AGC restoration and re-application.

Figures 7, 8, 9, and 10 show the CMP stacks for model B (Figures 7 and 8), and model E, respectively. Examination of these figures shows that model B and model E clearly differ in some important respect. Interestingly, the events near the right and left edges of Figures 7 and 8 appear to correlate with the stack images of model E in Figures 9 and 10, respectively; hence the physical models must be similar at least near the edges. Examination also reveals in Figures 7 and 8 that the centre portion of the section has a series of repeated strong events, most likely multiples created in the shallowest layers. We also see in these figures evidence that the reflection events have discontinuities near both edges, involving even the very shallowest reflection. This is strong evidence of a significant change in the properties of a shallow reflector near either end of the line, probably related to the 'time-lapse' simulation.

Based on the appearance of the section in Figures 7 and 8, we decided to remove multiples from the data set for model B, and to do it using a method introduced by Taner (1980).

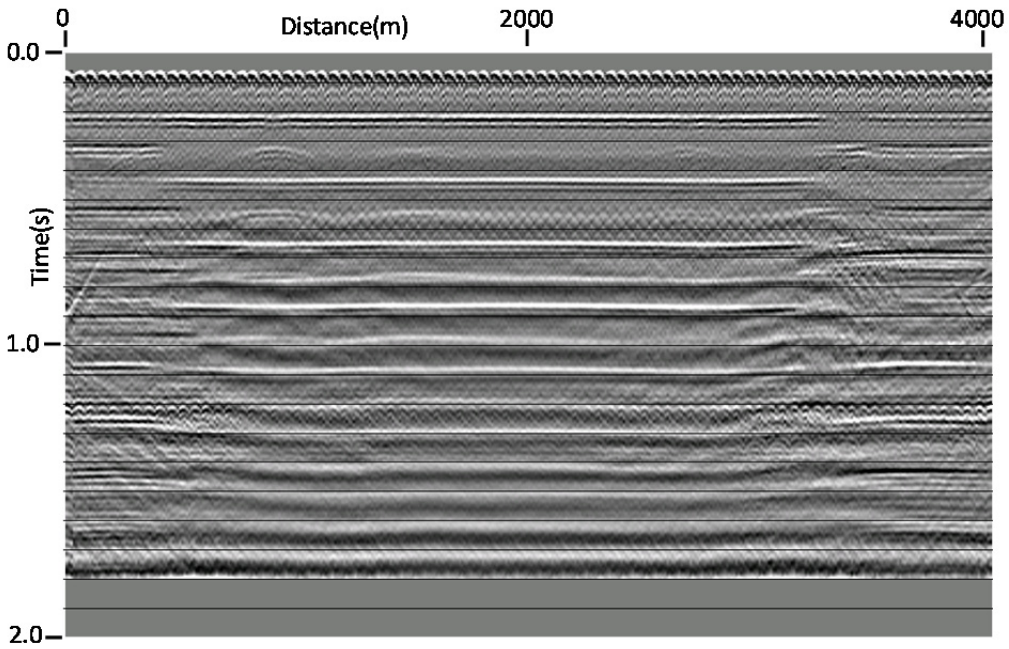

FIG. 7. CMP stack of Model B receiver line gathers after surface wave attenuation—centre of the section manifests apparent surface-related multiples.

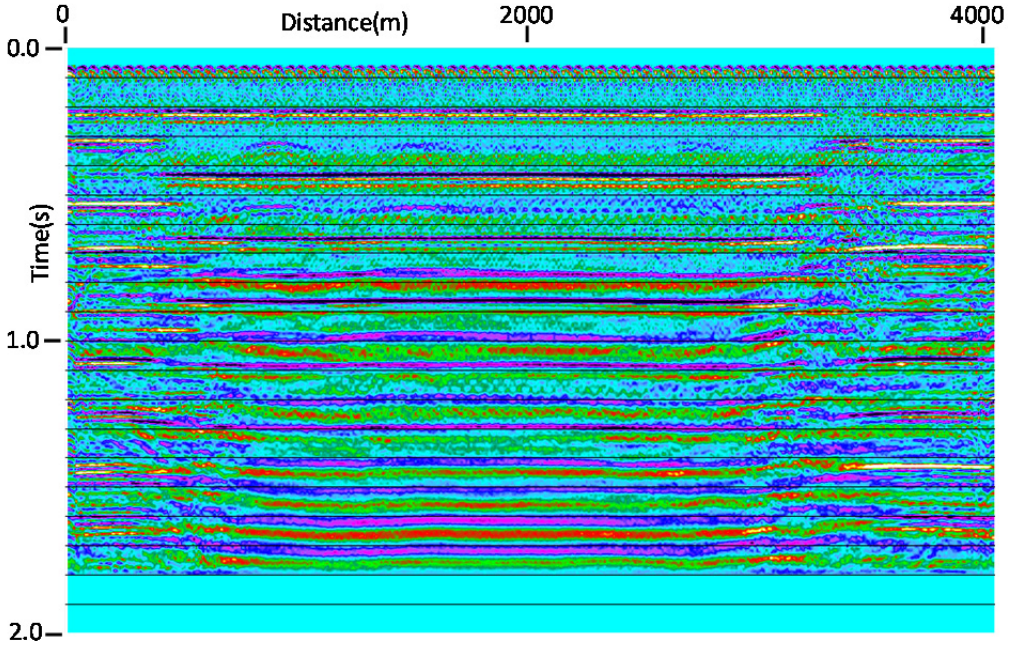

FIG. 8. Colour version of the Model B CMP stack in Figure 7.

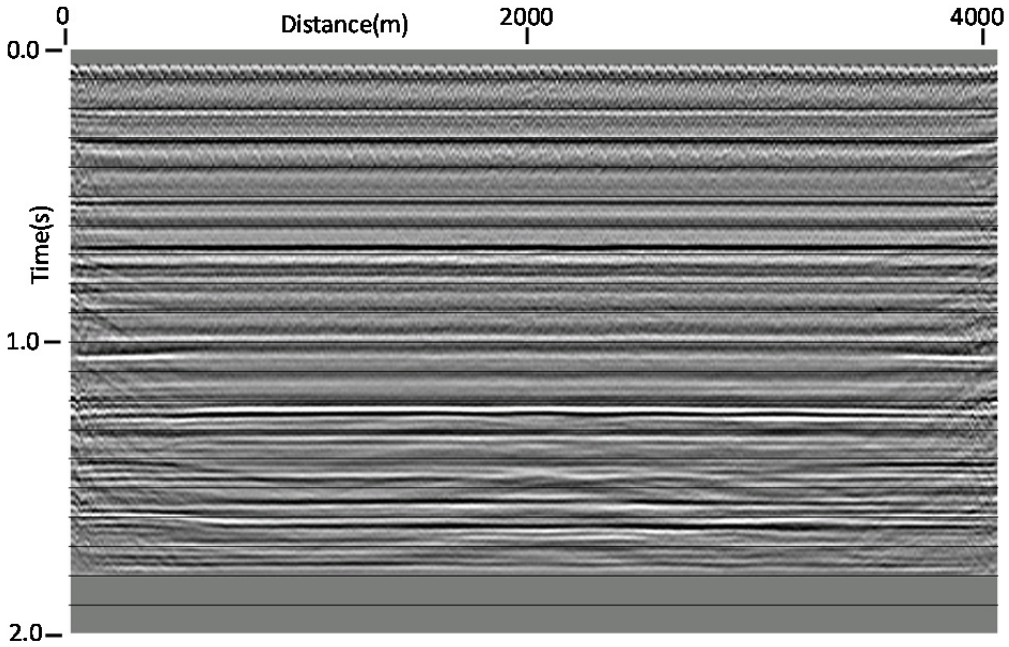

FIG. 9. CMP stack of Model E receiver line gathers after surface wave attenuation—no evidence of surface-related multiples.

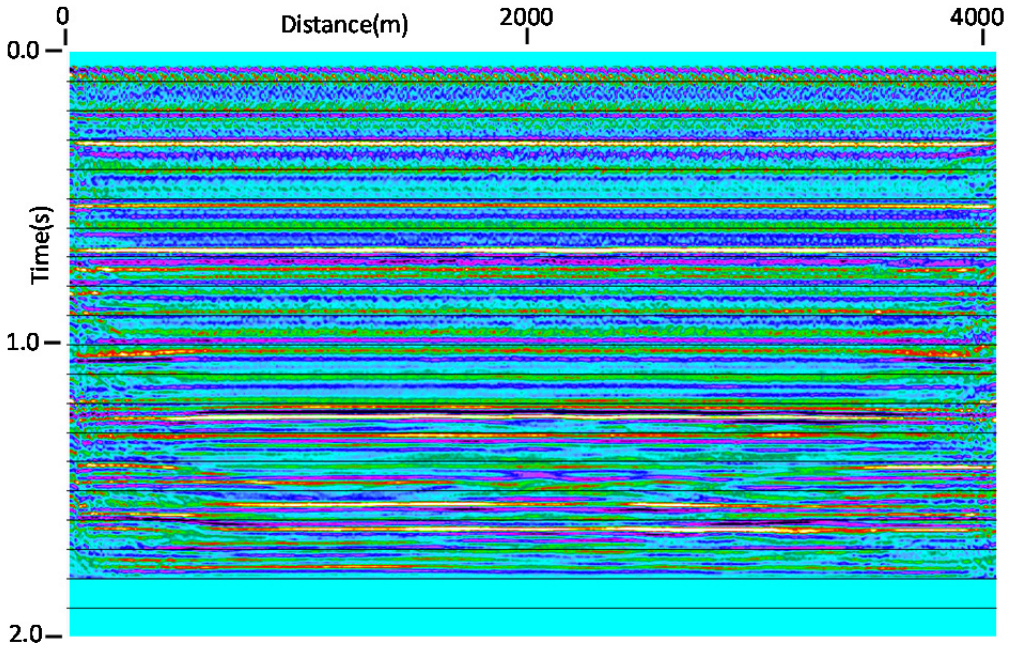

FIG. 10. Colour version of the Model E CMP stack in Figure 9.

De-multiple methods

As with any organized (or coherent) noise, we rely on certain characteristics of multiples to help separate them from legitimate single reflections. Figure 11 is a schematic portraying typical raypaths for simple reflections, as well as a raypath for a

shallow surface-related multiple. A distinguishing characteristic of surface-related multiples is the fact that their energy is confined to the shallower (and lower-velocity) portion of the earth. This means that a reflection associated with a deeper layer boundary will typically exhibit a higher normal moveout (NMO) velocity than a multiple occurring at the same traveltime. Hence, multiples and primary reflections may be separable on the basis of their NMO velocities. This is more generally true for surface-related multiples than for 'interbed' multiples associated with several bounces between deeper layer boundaries.

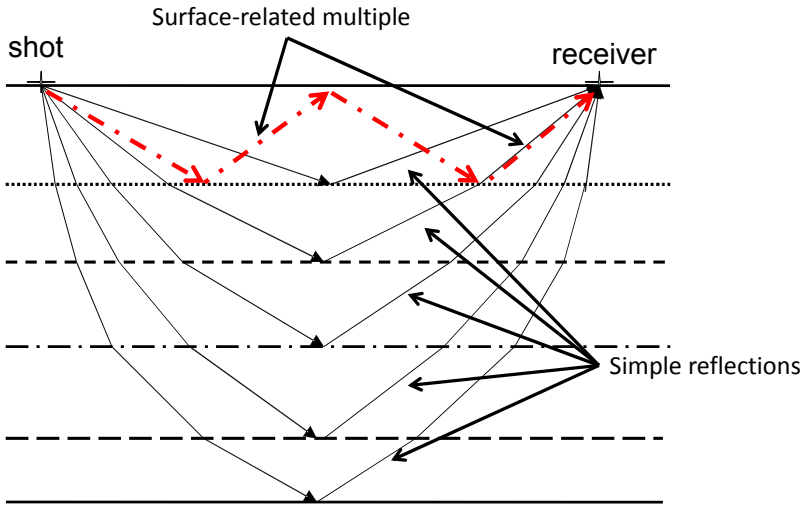

FIG. 11. Raypath diagram for a raw seismic trace from the conventional X-T domain.

One of the more successful NMO-based methods for attenuating multiples uses the Tau-P transform to enhance the separation of multiples from simple reflections, then mutes the multiples. Another method applies NMO to the raw data sufficient to flatten the multiple events, then uses an f-k transform to 'model' the multiple energy, which is then subtracted from the NMO-corrected gather before inverting the NMO correction. The former method can leave artifacts in the processed gather from the inverse Tau-P transform, while the latter usually damages legitimate reflections at the nearer offsets.

Another characteristic of multiples, especially surface-related multiples, is the reflection periodicity resulting from the repeated traverse of particular layers. In the case of marine data, water bottom multiples can often be observed for six or seven bounces, where the periodicity at zero offset is just the scaled water depth. For interbed multiples, if there are two or more bounces within the same layer, periodicity may appear in these events as well, though usually not as pronounced.

When the most distinct characteristic of a multiple is its periodicity, deconvolution methods are often used to attenuate it. Since periodicity in a time series leads to notches or peaks in its Fourier spectrum, any deconvolution method which attempts to whiten the spectrum will attenuate the multiple. Likewise, predictive deconvolution, based on the autocorrelation function of the time series can be used to remove the periodicity, and hence the multiple. Two flavours of predictive deconvolution can be used; the so-called 'gapped' deconvolution, in which a portion of the deconvolution filter in a 'gap' near

zero time lag is constrained to be zero, thus preserving the waveform of an event, and 'spiking' deconvolution, in which the unconstrained filter function both reduces periodicity and 'shortens' the event wavelet. Both these methods use autocorrelations of the input time series, which manifest the periodicity of multiples in the time series when the raypath geometry is most favourable.

Predictive deconvolution is actually based on the 1D convolutional model of the earth (zero offset), so when we attempt to apply it to seismic traces with any offset other than zero, it becomes less effective. Figure 12 shows why this is so for a simple surface-related multiple: in particular, the bounce points of the multiple don't coincide with the bounce point of the simple reflection for any offset except zero; and since the raypath angles are different for the multiple raypaths, so are the raypath segment lengths and corresponding traveltimes. Hence, for any offset other than zero, the timing of a multiple is no longer an integral multiple of that of the simple reflection. Both these offset-dependent effects diminish the effectiveness of de-multiple methods based on periodicity.

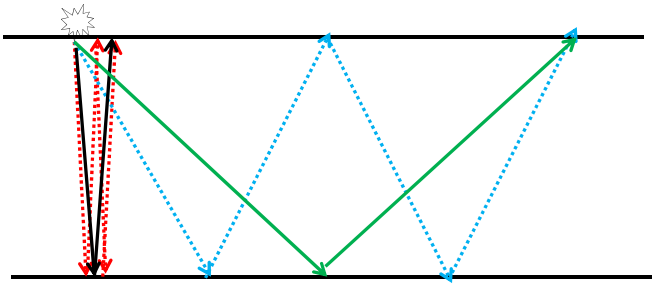

At near-zero offset, the surface-related multiple path (red) is nearly twice that of the primary reflection (black), and the reflection points are nearly the same; at longer offsets, the multiple path (blue) is significantly less than twice the primary path (green), and the reflection points are separated.

FIG. 12. Raypath diagram for conventional X-T seismic trace showing why the periodicity of surface-related multiples is disturbed as offsets increase.

Taner (1980) showed how transforming seismic data into the radial trace (RT) domain restored the periodicity of surface-related multiples and merged their bounce points with those of simple reflections, as well (Figure 13). This led to a successful de-multiple technique whose routine use required more computational resources than were available at the time. It is Taner's idea that we utilize in the current work.

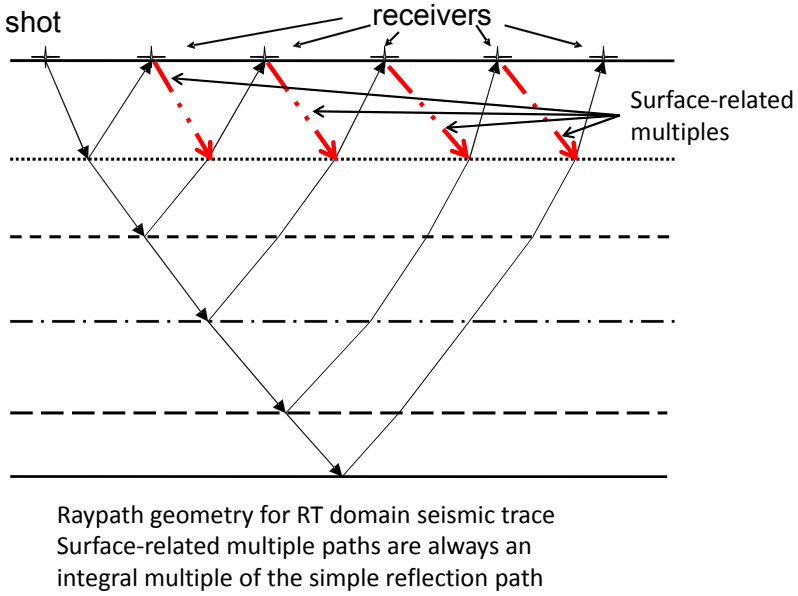

FIG. 13. Raypath diagram for seismic traces in the radial trace (RT) domain, showing that surface-related multiples retain their periodicity in this domain, and share some common reflection points with primary reflections.

RT domain de-multiple methods

There are two different approaches to de-multiple operations in the radial trace domain, depending upon whether or not NMO correction is applied to the trace gather before transforming it to the RT domain. We tested both, and present the results below.

One of the properties of the radial trace transform, as shown by Taner (1980), is that for primary reflections and their surface-related multiples, the periodicity of the multiples is restored during the RT transform, as long as the moveout velocity of the multiples is the same as that of the primary (guaranteed by the surface-related multiple raypath geometry shown in Figure 13). Also, since the RT transform is a simple remapping operation, the relative amplitudes of the multiples are preserved; although this consideration appears to be less important than event kinematics and proper polarity. On the other hand, if we apply NMO to the entire trace gather before the RT transform, *using only the moveout velocity of the primary reflection*, the multiple event kinematics are still preserved, since all events with the same moveout as the primary will be flattened, and the event timing at zero offset is propagated to all offsets. The main difference in this approach is that NMO stretch appears in both the primary and multiples and may affect de-multiple operations.

NMO correction before de-multiple

We determined the NMO velocity for the prominent reflection at 200ms on the model B data set and applied it at all travel times. Figure 14 shows one of the resulting shot gathers, and Figure 15 is its RT transform. In Figure 14, not only is the periodicity of the multiple evident, but we observe that the events all appear to be tilted slightly down to the right. This may be due to a slight variation in thickness of the top layer of the physical

model, or to a consistent source coordinate error, but we corrected it by simply modifying the 'offset' trace headers by adding a constant value. As a result of the trace header correction, the RT transform in Figure 15 shows no such event tilt. The periodicity of the 200ms reflection and its multiples is quite evident in this display, but we note that for ray parameters less than about -3500m/s or greater than 3500m/s, the ray angle is too shallow to capture any of the multiples, and hence to derive de-multiple operators. Although not required for the de-multiple operation, we sorted the RT transforms to the domain of ray parameter and source location to make common-ray-parameter panels (Henley, 2008, 2010, 2012), like the one displayed in Figure 16 for a ray parameter of -2001m/s. On Figure 15, the position of the -2001m/s trace is noted. As is typical for common-ray-parameter panels, the S/N of the events is higher than on the original shot gathers, and the periodicity of the 200ms reflection and its simple one-bounce surface multiple is very evident. Referring back to Figure 15, we can see, as well, that the -2001m/s trace does not include any of the higher order multiples that would be seen by traces corresponding to steeper ray parameters. The common-ray-parameter panel for -600m/s, in Figure 17, for example, exhibits the periodicity of the higher order surface multiples.

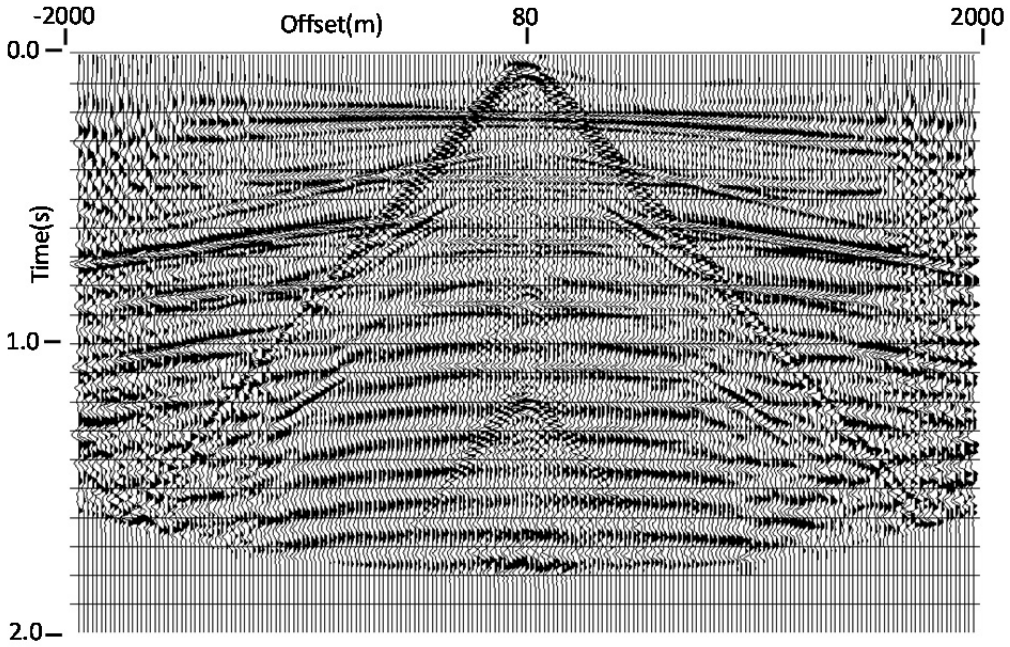

FIG. 14. The receiver line gather from Figure 5 after application of NMO for a constant velocity that matches the reflection at 200ms and its multiples. Note the tilt in this reflection—likely due either to a slight linear variation in thickness of the top-most physical model layer, or to a consistent source coordinate error.

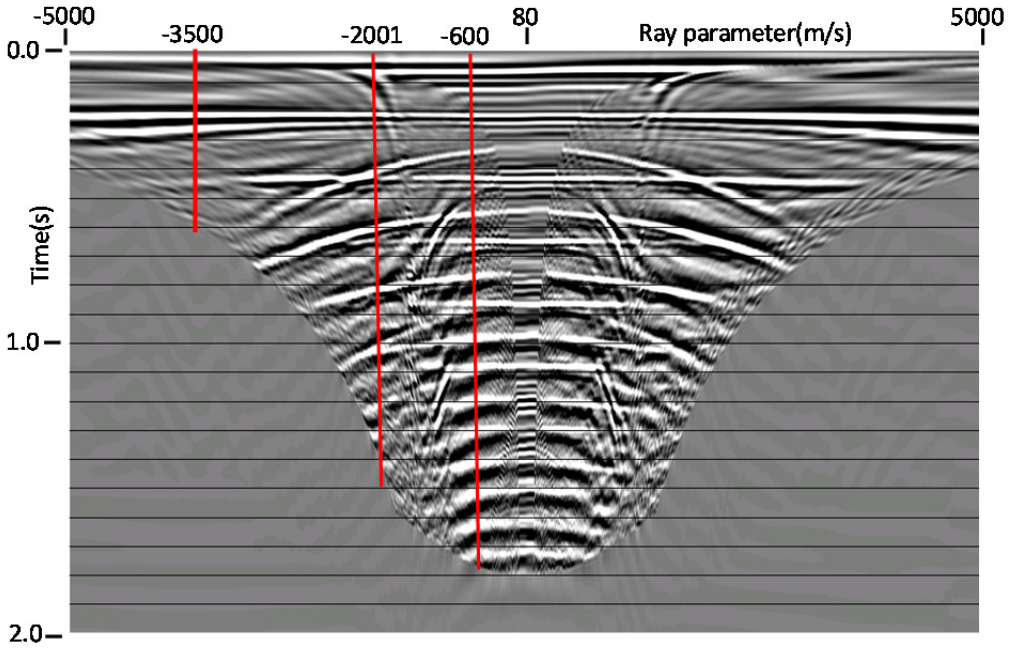

FIG. 15. Radial trace (RT) transform of the gather in Figure 14. The periodicity of the 200ms reflection and surface-related multiples is evident. Trace header corrections on the raw receiver gather have removed event tilt. Radial traces at three different ray parameters are flagged.

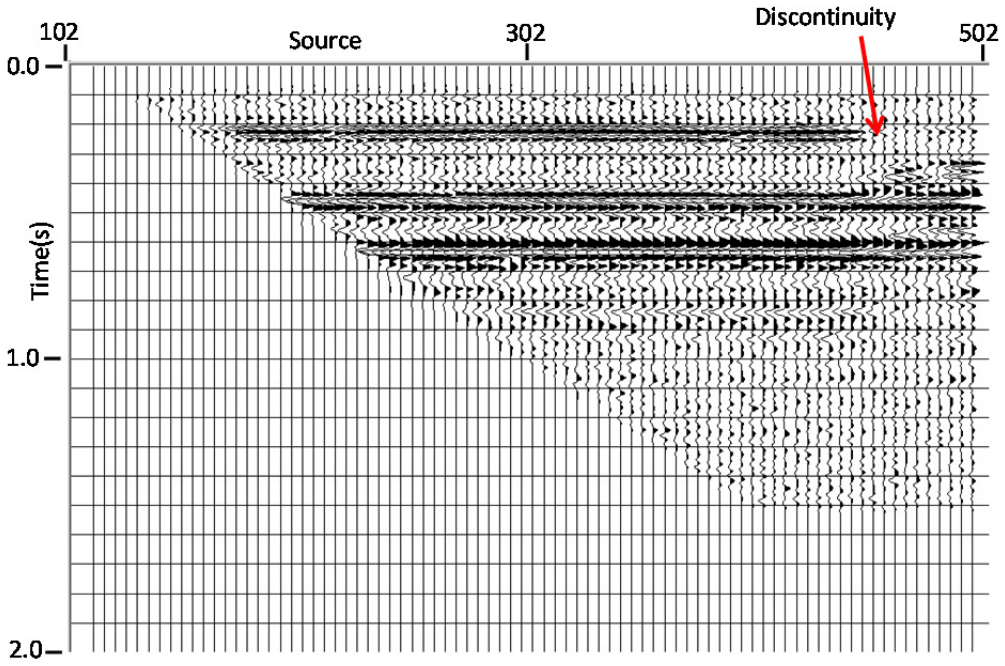

FIG. 16. Common-ray-parameter gather for Model B at ray parameter = -2001m/s. All traces with this ray parameter have been extracted from the RT transforms of the receiver line gathers of Model B and sorted by source location. Note reflection discontinuity of 200ms event.

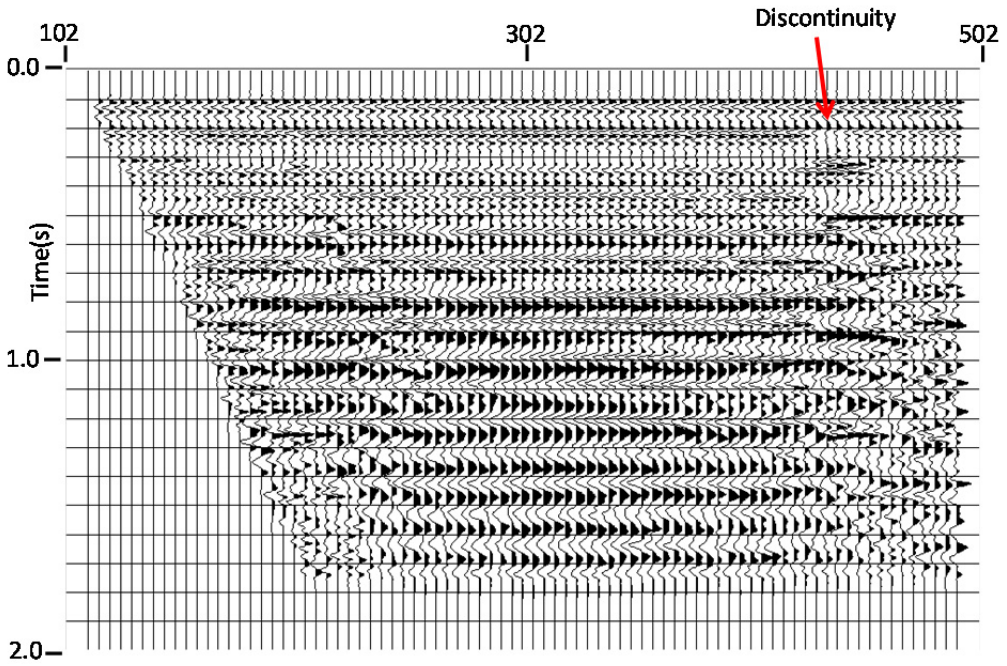

FIG. 17. Common-ray-parameter gather for Model B at ray parameter = -600m/s. For this ray parameter, multiple periodicity is much more evident. Discontinuity of 200ms reflection is evident on this gather, as well.

We chose Taner's (1980) technique for attenuating multiples, based on apparent periodicity. Autocorrelations were first computed for all the common-ray-parameter panels—Figures 18 and 19 show the autocorrelations for the common-ray-parameter panels at -2001m/s and -600m/s, respectively. The autocorrelations in both cases highlight the periodicity of the multiples, particularly for the -600m/s ray parameter. Conventional spiking deconvolution was used to derive inverse filters from all the autocorrelations on all common-ray-parameter panels. Gapped deconvolution, a variation of spiking deconvolution in which a few samples following the first sample of the operator are zeroed, could also be used, but our results were better for a full spiking deconvolution. When the appropriate inverse filter operators were applied to the input common-ray-parameter panels, the multiples were very effectively reduced, as shown in Figures 20 and 21 for ray parameters -2001m/s and -600m/s, respectively (compare with Figures 16 and 17). As further confirmation, we autocorrelated the deconvolved common-ray-parameter panels, and note the reduced periodicity in Figures 22 and 23 for ray parameters -2001m/s and -600m/s, respectively, compared to Figures 18 and 19.

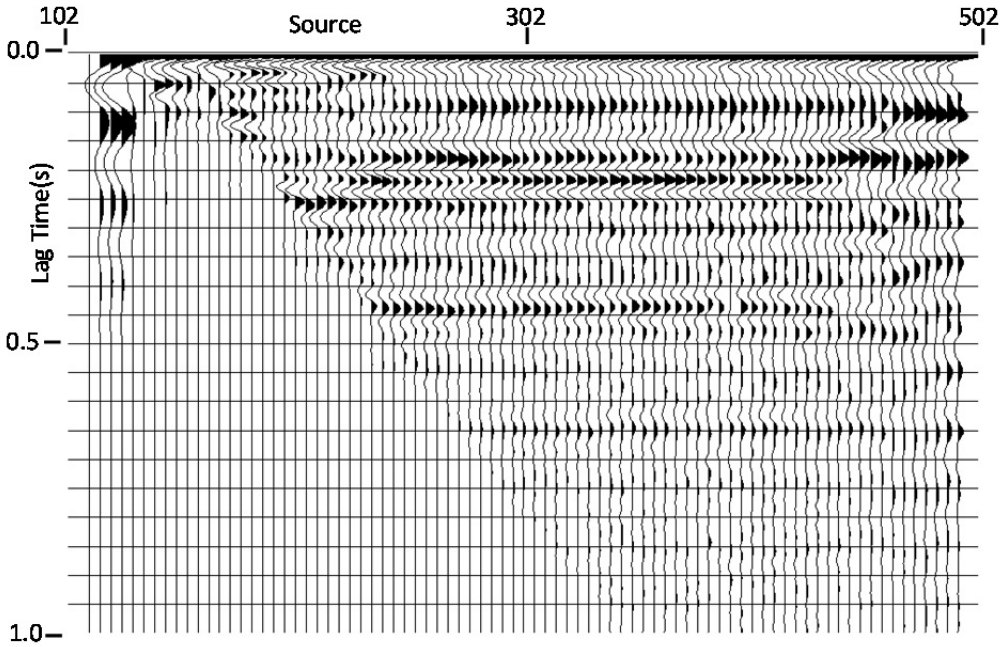

FIG. 18. Autocorrelation functions for the common-ray-parameter gather at -2001m/s.

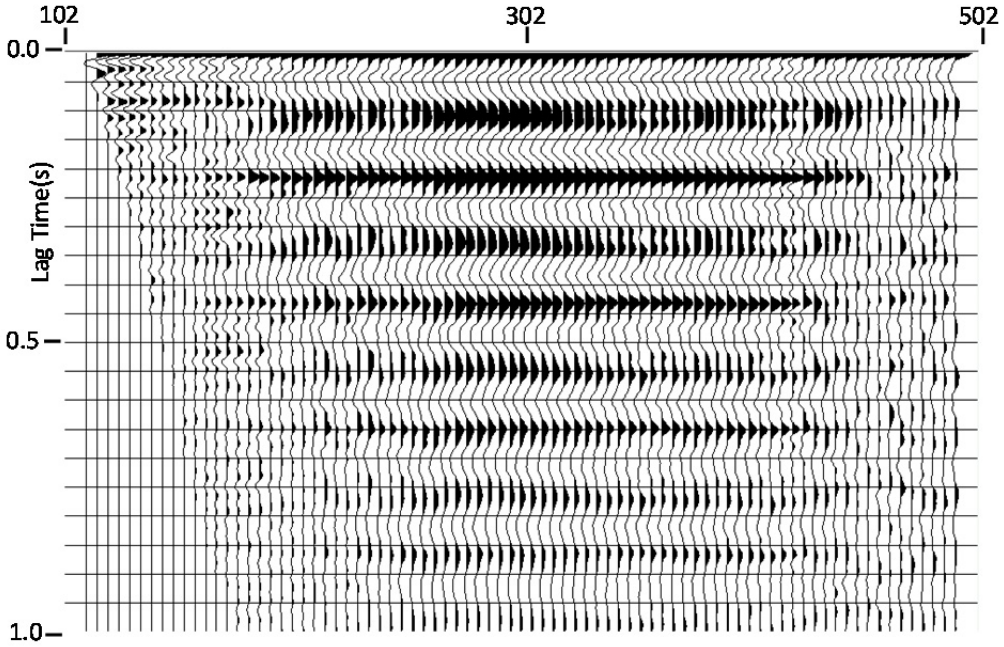

FIG. 19. Autocorrelation functions for the common-ray-parameter gather at -600m/s.

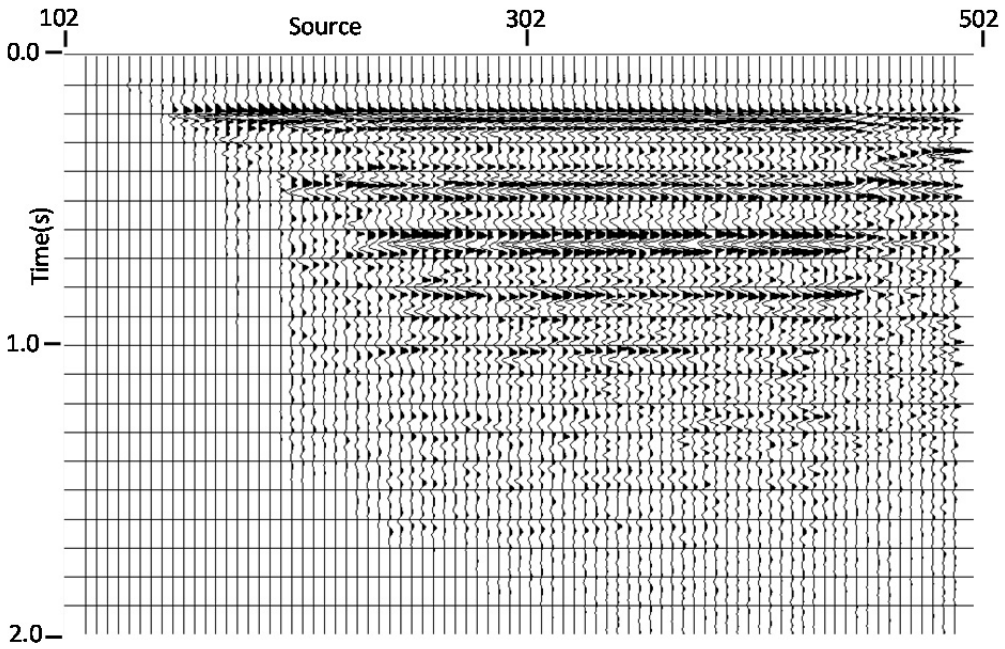

FIG. 20. Common-ray-parameter gather after spiking filter based on autocorrelation functions in Figure 18. Compare with Figure 16 to verify decreased multiple amplitudes.

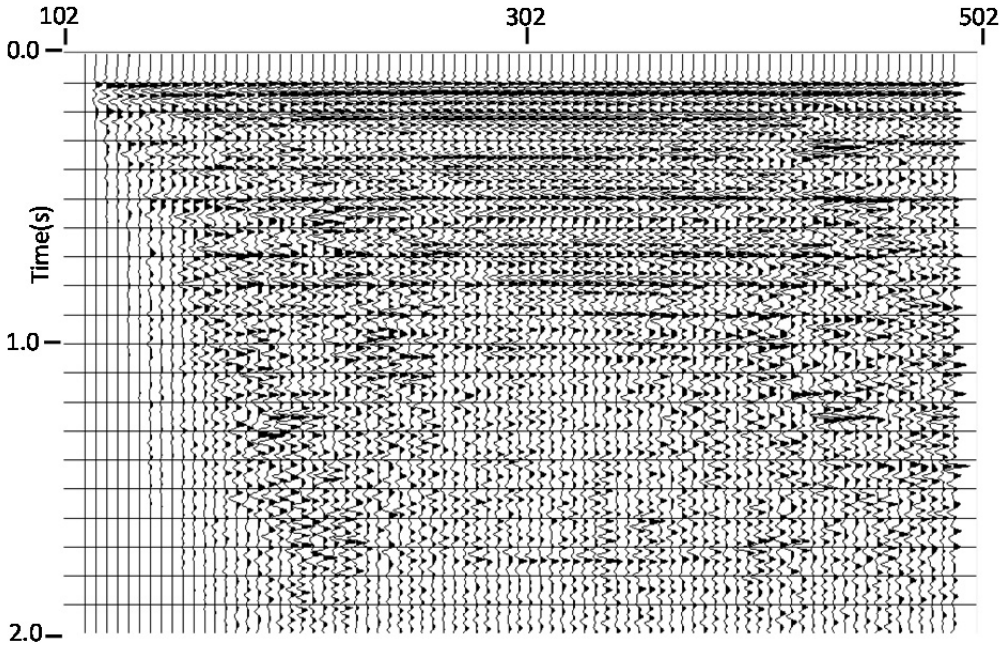

FIG. 21. Common-ray-parameter gather after spiking filter based on autocorrelation functions in Figure 19. Compare with Figure 17 to verify decreased multiple amplitudes.

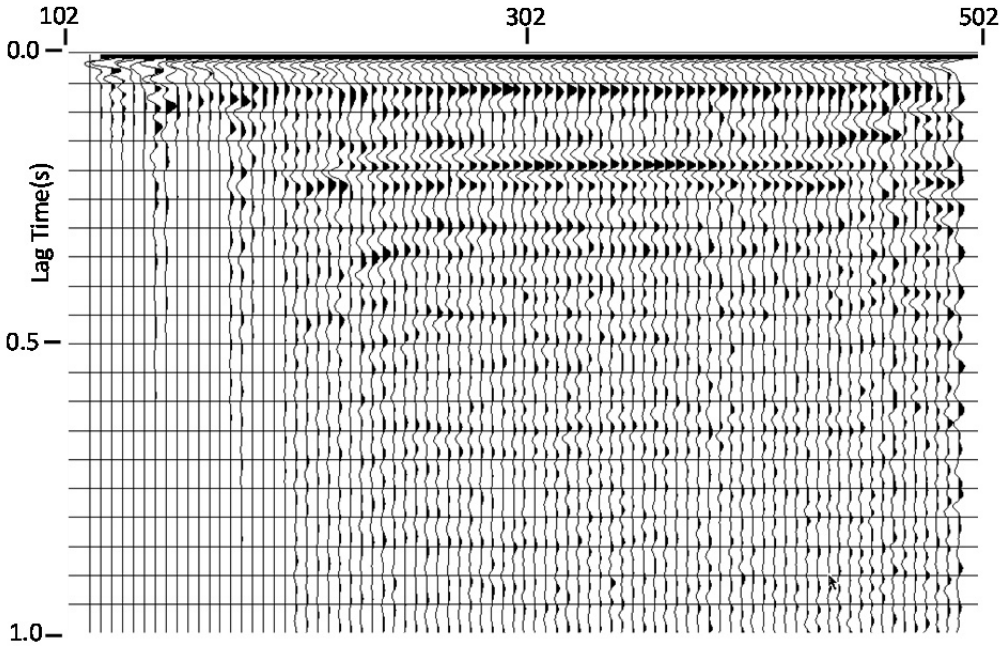

FIG. 22. Autocorrelations for common-ray-parameter -2001m/s after application of spiking filters. Side lobes are reduced compared to Figure 18.

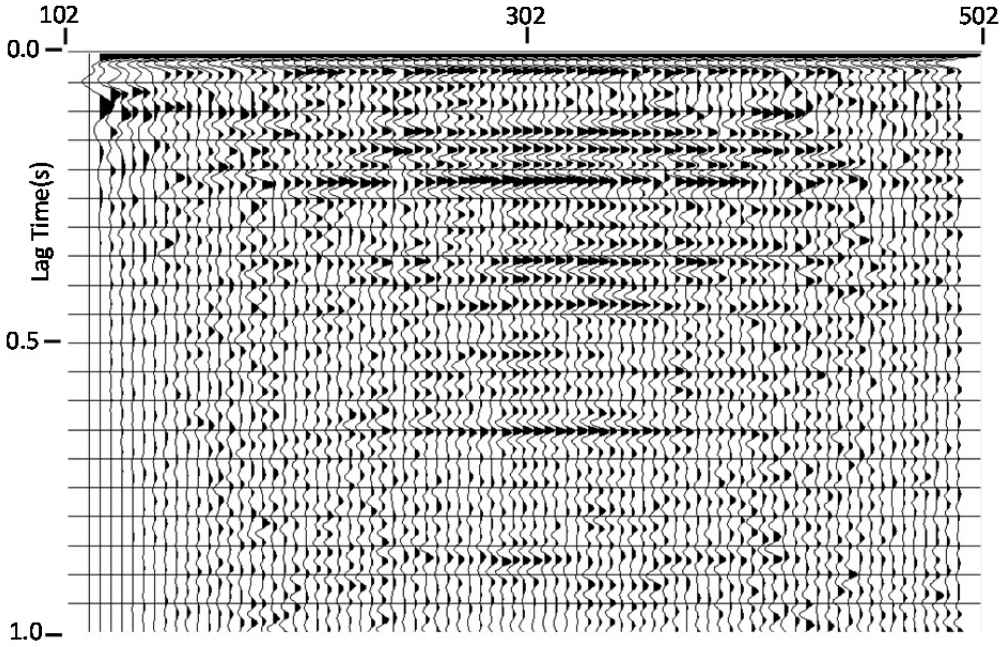

FIG. 23, Autocorrelations for common-ray-parameter -600m/s after application of spiking filters. Side lobes are much reduced compared to Figure 19.

After the de-multiple operation, the data were sorted back into RT transforms (Figure 24). The inverse RT transform, followed by inverse NMO correction (to remove the effects of the original constant-velocity NMO operation) converts them back to shot

gathers (Figure 25). Applying the full NMO function (for all reflections) to the shot gathers and forming the CMP stack results in Figures 26 and 27, which can be compared with Figures 7 and 8, respectively.

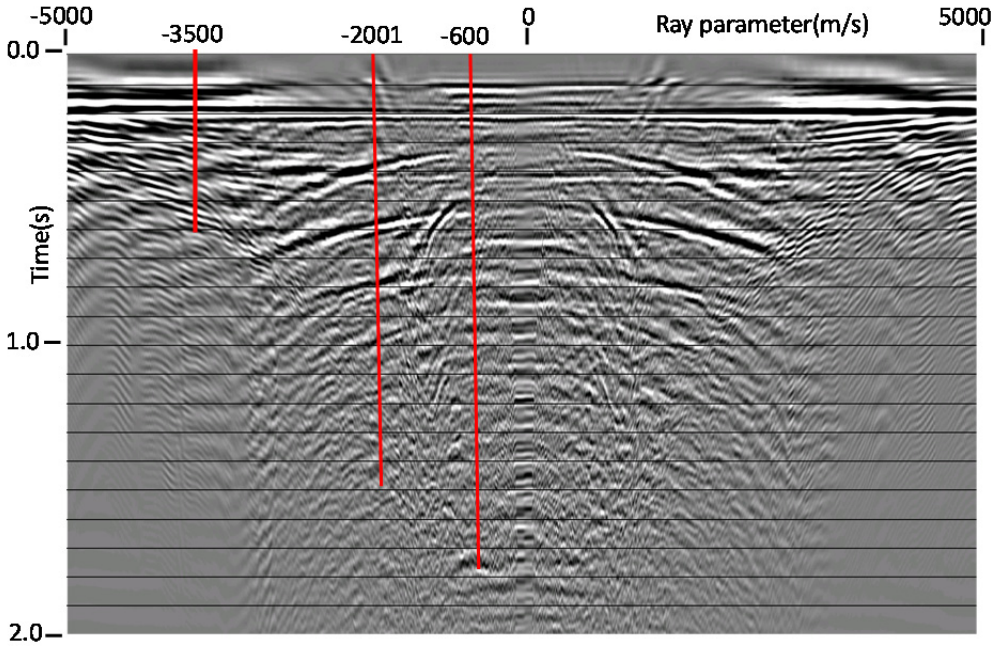

FIG. 24. RT gather recovered by sorting from common-ray-parameter gathers after spiking filters applied. Comparing with Figure 15, note the large decrease in multiple amplitudes, while hyperbolic events (other reflections) remain largely intact.

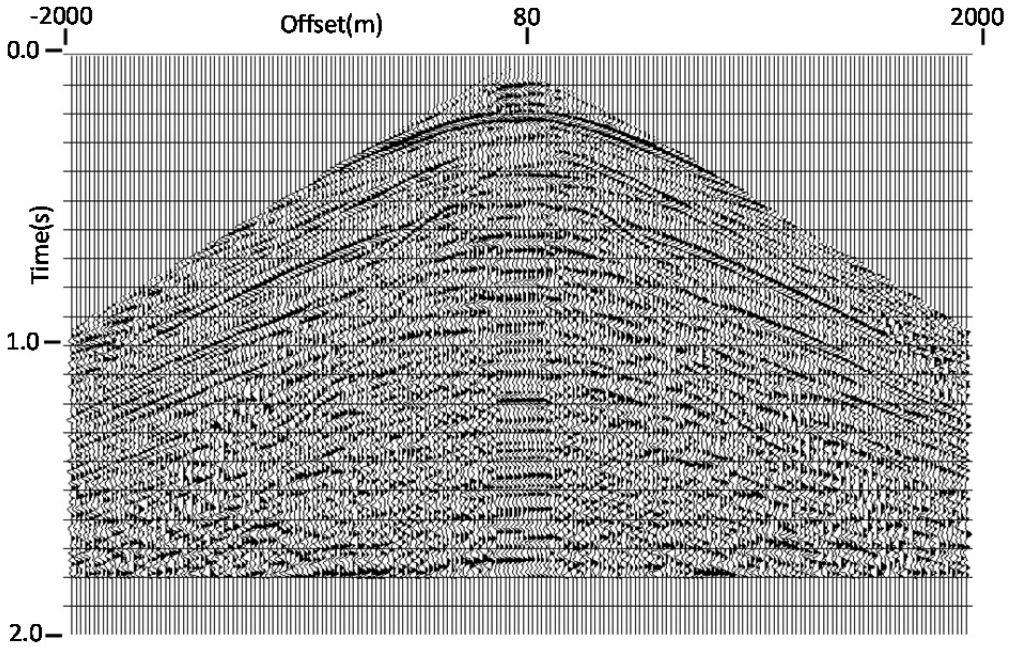

FIG. 25. Inverse RT transform of the RT gather in Figure 24, followed by restoration of the NMO leads to this de-multipled receiver line gather.

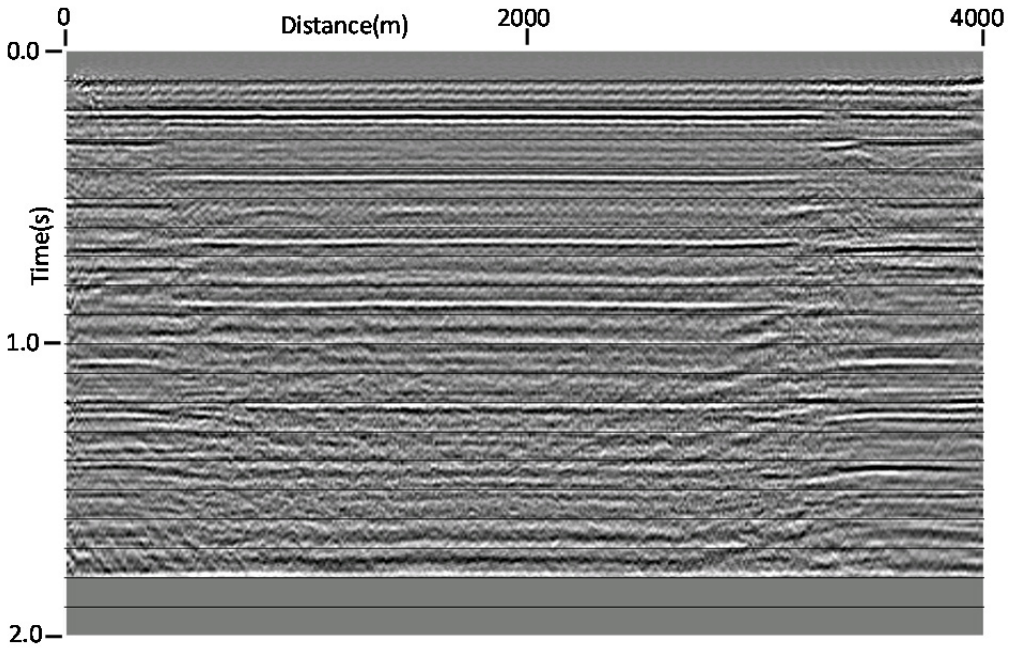

FIG. 26. CMP stack of Model B after de-multiple of receiver line gathers.

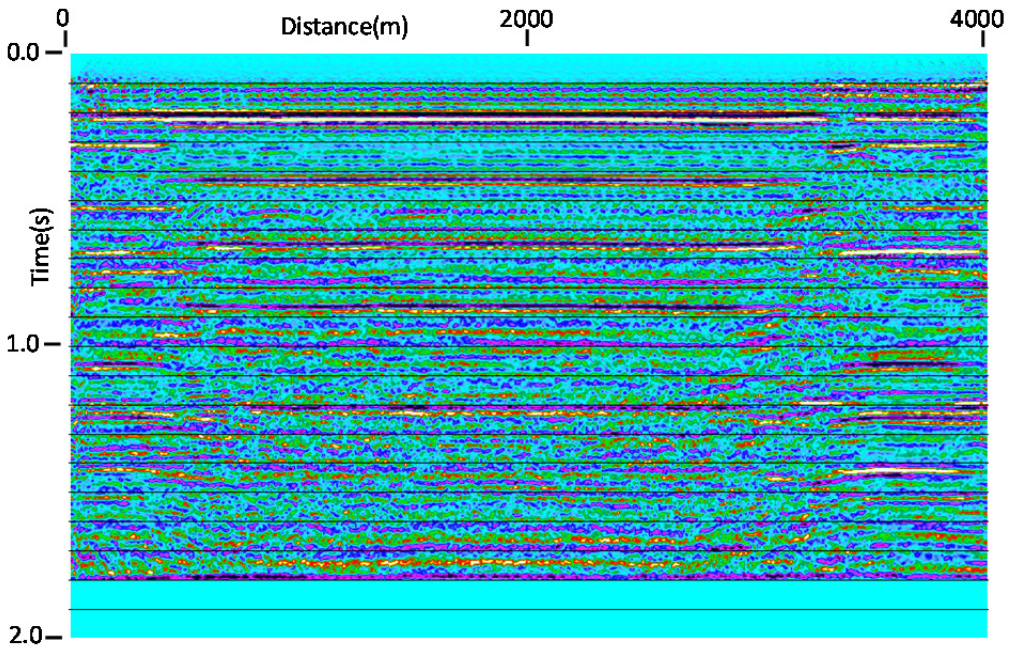

FIG. 27. Colour version of the Model B CMP stack in Figure 26.

No NMO correction before de-multiple

In this case, we transformed the model shot gathers directly to the RT domain, with no NMO correction, as in Figure 28. Thanks to the geometry of the RT transform, primary reflections and their surface-related multiple events remain nearly periodic in time over a significant range of ray parameters regardless of the moveout of the event and its multiples. Examination of Figure 28 appears to verify this for more than half of the displayed range of ray parameters. While there is no explicit wavelet stretch induced by NMO correction, events like the 200ms reflection are stretched, nevertheless, due to their increasing slope in the RT domain, near the extremes of the ray parameter range. This happens when the RT sample trajectories in the X-T domain approach tangency with the event wavefronts. Since the worst of this stretching occurs for ray parameters at which multiples are not present, the problem is not significant. We next sorted the data to common-ray-parameter panels to look for periodicity, as in the previous technique. In this case, because of the presence of NMO, we recall that events which appear flat on the common-ray-parameter panels will shift in time between panels, due to the moveout difference for different ray parameters. Figure 29 shows a common-ray-parameter gather for -1504m/s, and we can immediately see the periodicity of the primary reflection (at 300ms on this panel) and its simple surface multiple. The autocorrelations for this panel, in Figure 30, confirm the periodicity. Spiking deconvolution filters derived from these autocorrelations and applied to the common-ray-parameter panel yield Figure 31, in which multiple amplitudes are much reduced. The autocorrelation and spiking deconvolution can be iterated to reduce multiple amplitudes even further, as in Figure 32. When the processing is completed through the CMP stack stage, the single-pass de-multiple yields Figure 33, while the iterated de-multiple process gives Figure 34.

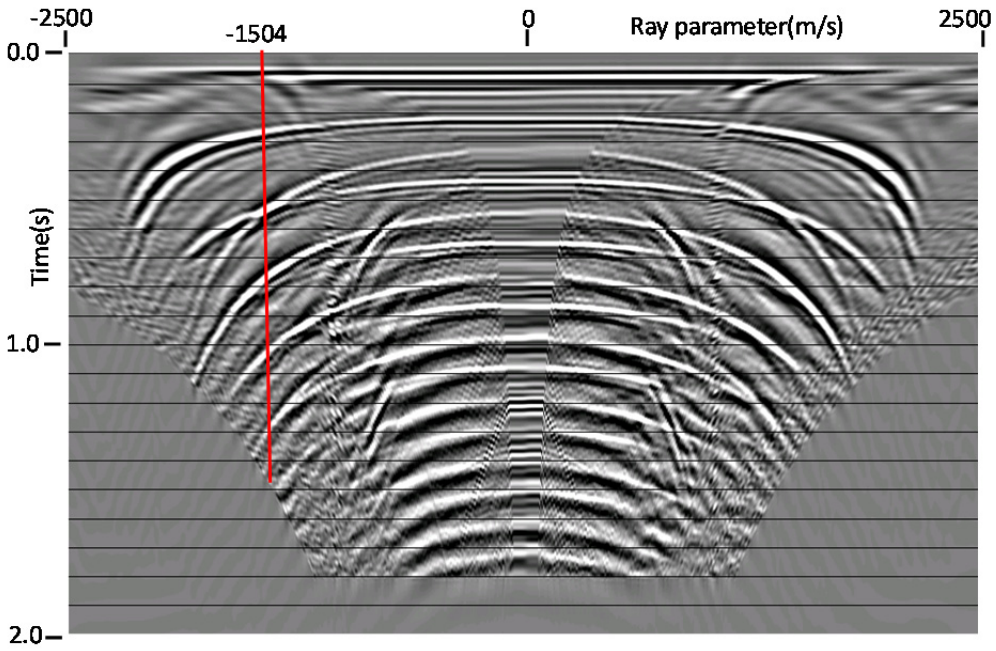

FIG. 28. RT transform of receiver line gather from Model B with no NMO correction before transform operation. Trace at ray parameter = -1504m/s is highlighted.

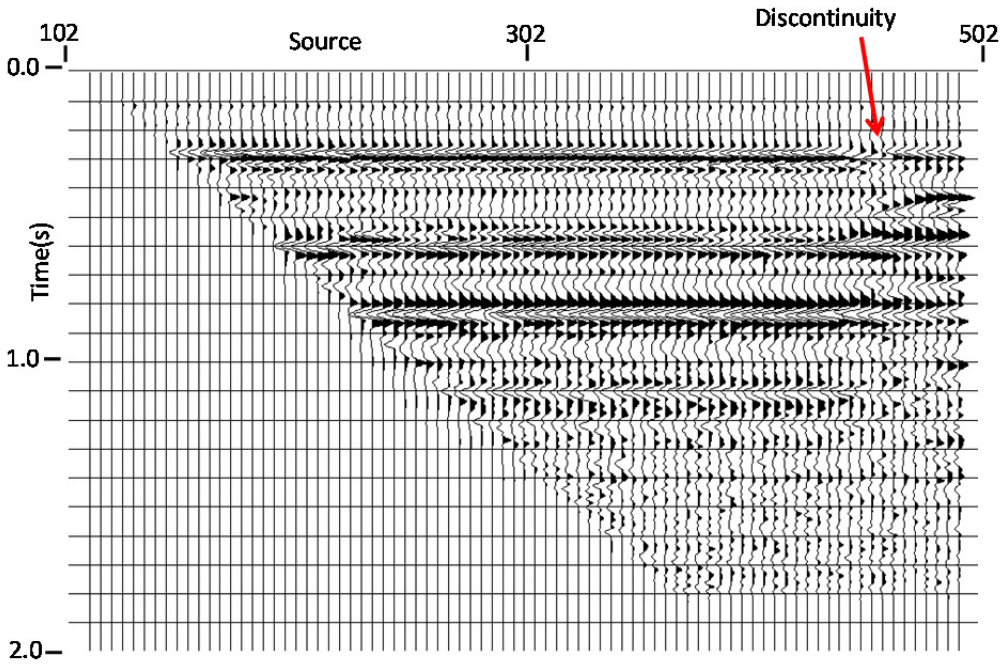

FIG. 29. Common-ray-parameter gather for ray parameter = -1504m/s. The discontinuity in the 200ms reflection is visible on this gather, as it was for the gathers in Figures 16 and 17.

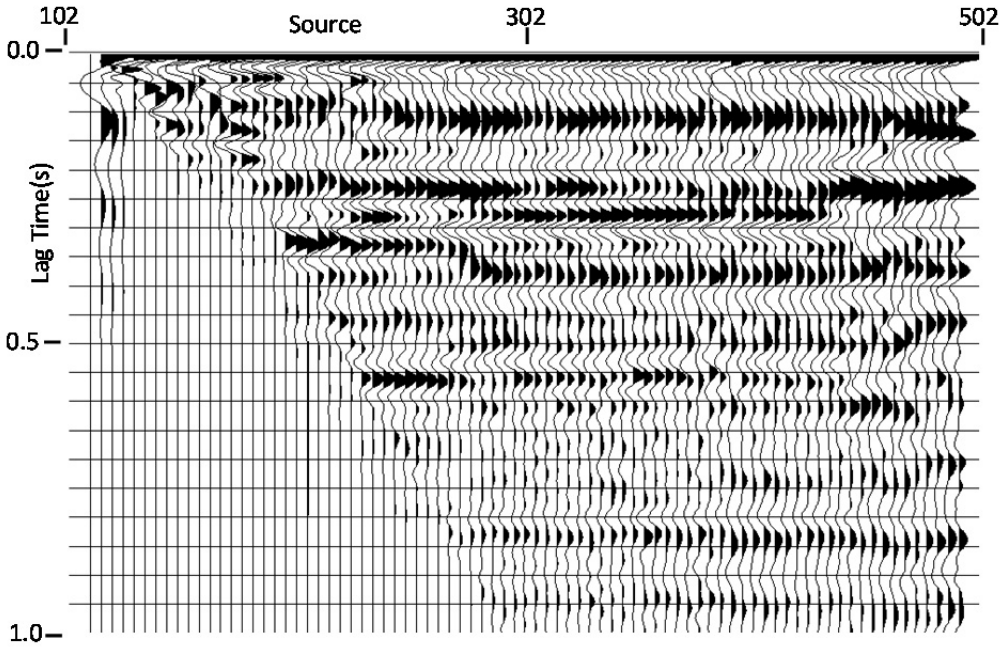

FIG. 30. Autocorrelation functions for the gather in Figure 29.

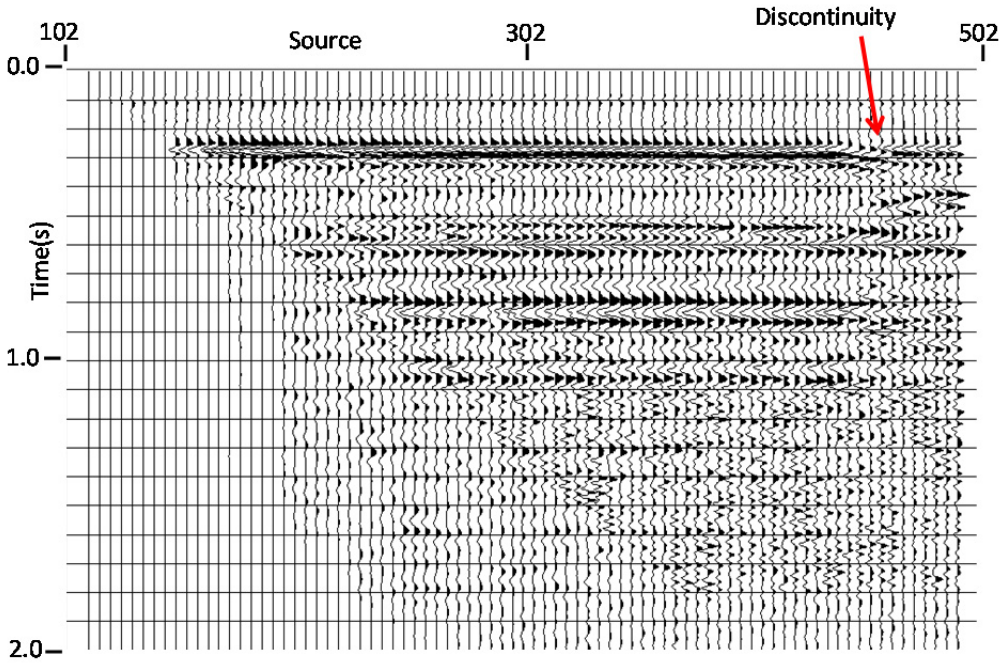

FIG. 31. Common-ray-parameter gather for -1504m/s after spiking filters based on autocorrelations in Figure 30. Multiple amplitudes are significantly reduced.

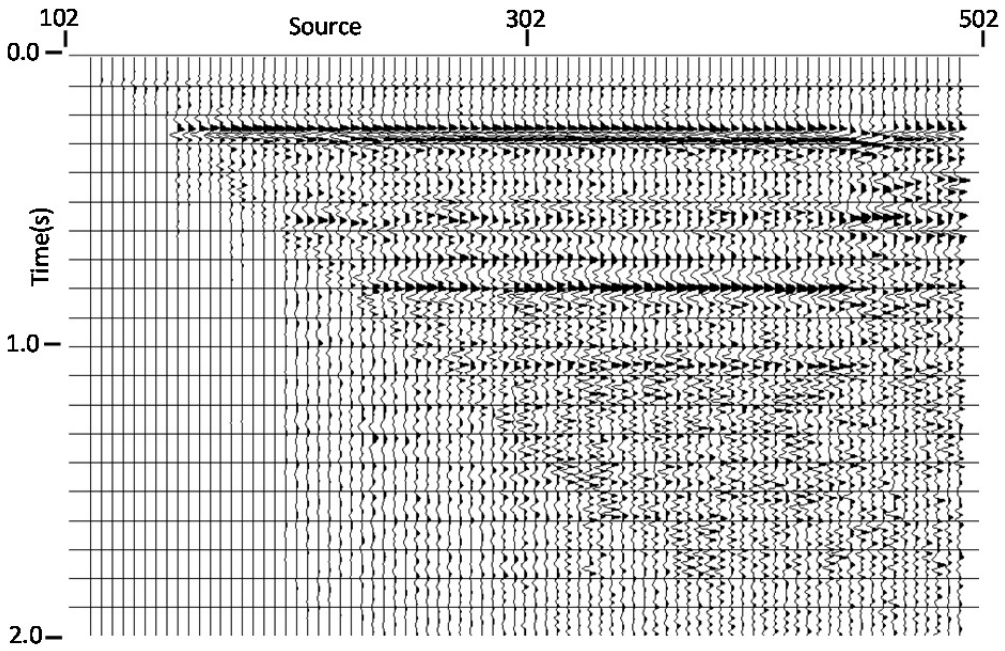

FIG. 32. Common-ray-parameter gather at -1504m/s after two cycles of autocorrelation and spiking filter application. Multiples are further reduced, but noise is increased.

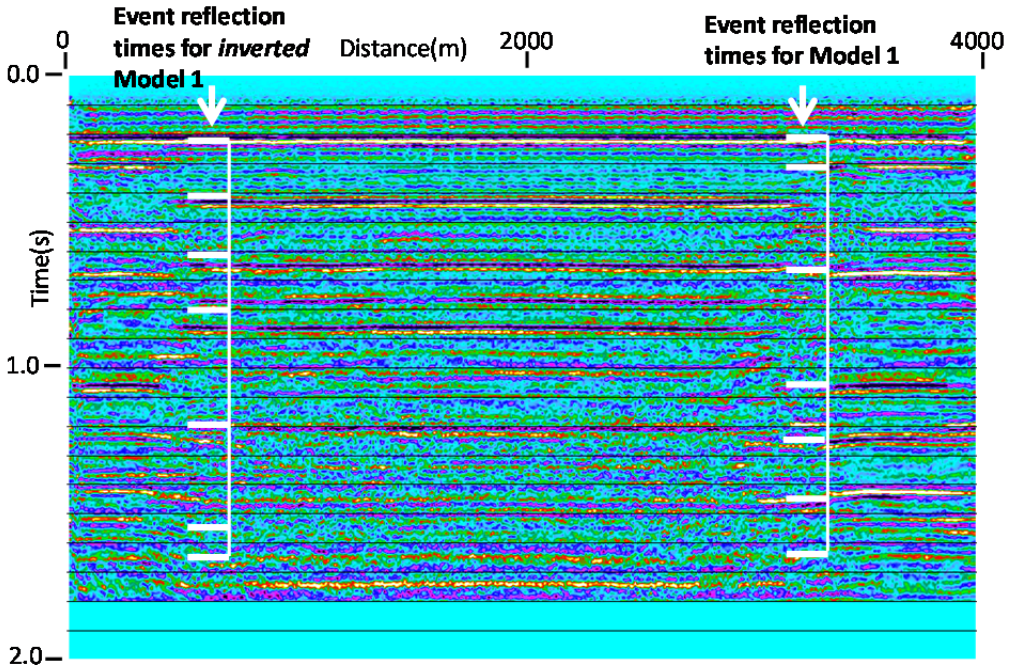

FIG. 33. CMP stack of Model B after one pass of de-multiple in RT domain with no NMO application before de-multiple. Zero-offset reflection traveltimes for two possible physical model configurations are superimposed.

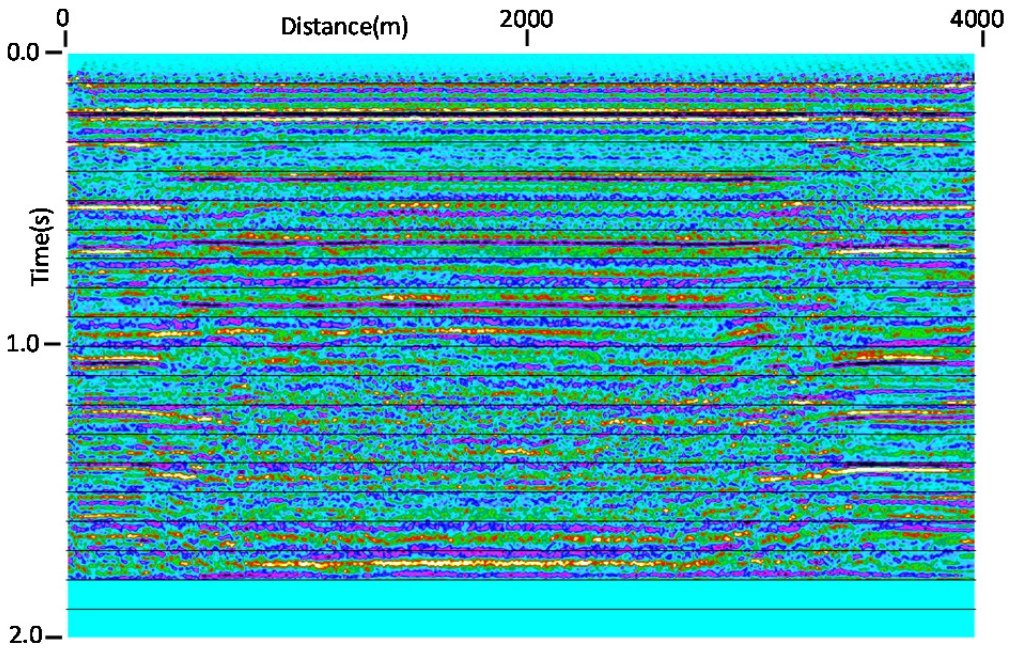

FIG. 34. CMP stack of Model B after two passes of RT-domain de-multiple. Multiple amplitudes are further diminished, but random noise is increased.

Comparing the processes

When we compare the images in Figures 26 and 27 with that in Figure 33, it is difficult to tell which de-multiple process works best. We attempted several variations on each procedure, in some cases trying to honour the time-scaled amplitudes of the multiples when deriving the spiking deconvolution operator (the theoretically correct approach), and in others trying to boost the multiple amplitudes in order to emphasize the multiple periodicity. Ultimately, what seemed to work best for amplitudes, whether applying de-multiple before or after moveout correction, was to apply AGC before RT filtering, remove this AGC from the filtered data, then apply a new AGC to the de-noised data prior to transforming it to the RT domain for the de-multiple procedure. The autocorrelations computed for the common-ray-parameter panels when this amplitude procedure had been performed on the original shot gathers seemed to give the best representation of the *periodicity* related to the surface multiples, and hence led to the best spiking deconvolution operators. Over-emphasizing the amplitudes of multiples by means of sample squaring or other non-linear operations on the autocorrelation functions can lead to more aggressive spiking deconvolution operators, which will further attenuate surface multiples; but legitimate reflection amplitudes also suffer. Iterating the autocorrelation and estimation procedure on each common-ray-parameter panel can improve the de-multiple results marginally, but S/N seems to suffer for legitimate reflections.

Comparing the models

In order to equitably compare model E with model B, we applied the same de-multiple process to the model E shot gathers, even though there were no apparent surface-related multiples in the data for this model. We used the pre-NMO de-multiple procedure and

obtained the CMP stack for model E shown in Figure 35. In order to more easily compare this image visually with the CMP image for model B, we plotted the two side-by-side in Figure 36, with a compressed horizontal scale. Clearly, Model E on the right provided a much clearer image than model B, exhibiting continuous reflection events across the entire model. Since all of the strong events on model E match events at the edge of model B, we concluded that the underlying 'baseline' and 'time-lapse' versions of the physical model are either identical or very similar at the edge. Nevertheless, we see abrupt changes in model B as we move in from either edge, and the centre section shows distinct differences from model E. These differences are apparent for most of the traveltimes on the section, so the actual model differences at the very least originate in one of the shallower layers. We also see that whatever shallow feature is present in model B generates surface-related multiples, and seems to attenuate legitimate seismic reflections transmitted through it.

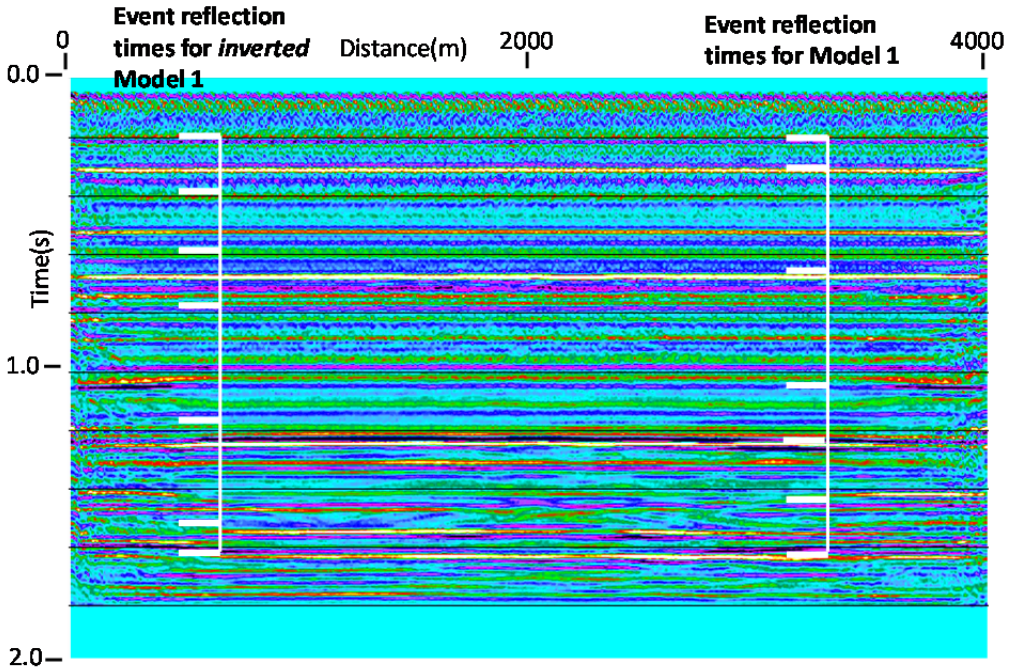

FIG. 35. CMP stack of Model E after one pass of RT-domain de-multiple. Very little effect of the de-multiple operation is visible, comparing with Figure 10. Zero-offset reflection traveltimes for two possible physical model configurations are superimposed.

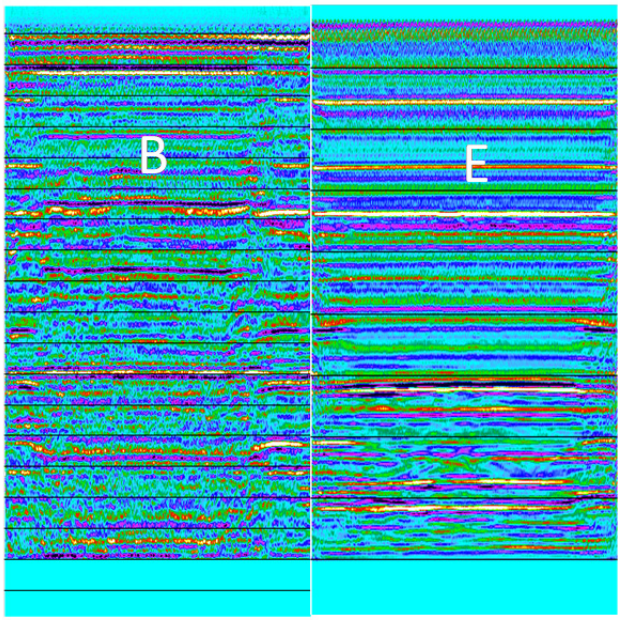

FIG. 36. CMP stack images for Models B and E compared side-by-side. Model B matches Model E relatively well at the edges, but S/N is lower.

Selecting the correct physical model

The physical model used for this processing study was not disclosed to the Processor until several CMP images had been produced for each 'baseline' and 'time-lapse' model. At that point, the model schematic in Figure 37 was presented to the Processor by the Modeller, who asserted that this diagram described model B, and that model E differed only in the replacement of the Teflon target in the lower part of the model with a continuous water layer.

If models B and E were as represented in Figure 37, we would expect the upper portions of both images to be very similar in appearance across most of the image, and to exhibit similar S/N. The only significant image differences should be in the lower part of the images. This not what we actually observe in Figure 36, however. Furthermore, when we tried to match reflection events on the images in Figures 33 and 35 with specific layer boundaries in Figure 37, the zero-offset event traveltimes matched significant events at the edge of Figure 33, as well as the continuous reflections on Figure 35; but there was only a poor match in the centre of Figure 33. These observations, as well as the discontinuities observed in shallow reflection events during the de-multiple processing, led the Processor to reject the model depicted in Figure 37 as the one actually surveyed for this study. In fact, the Processor suggested that the images might be more consistent with this physical model *if the model had been inverted in the physical modeling facility*, so that the removable Teflon block would have been near the model's upper surface! This hypothesis failed, however, because zero-offset traveltimes computed from the inverted model diagram, while matching some of the events in the centre portion of Figure 33, then failed to match events near the edge, or to match the continuous events on Figure 35.

FIG. 37. Candidate model No. 1--considered for compatibility with processed images for Model B and Model E—Model E obtained by replacing Teflon with continuous water layer. This model was rejected, based on inconsistencies with the images.

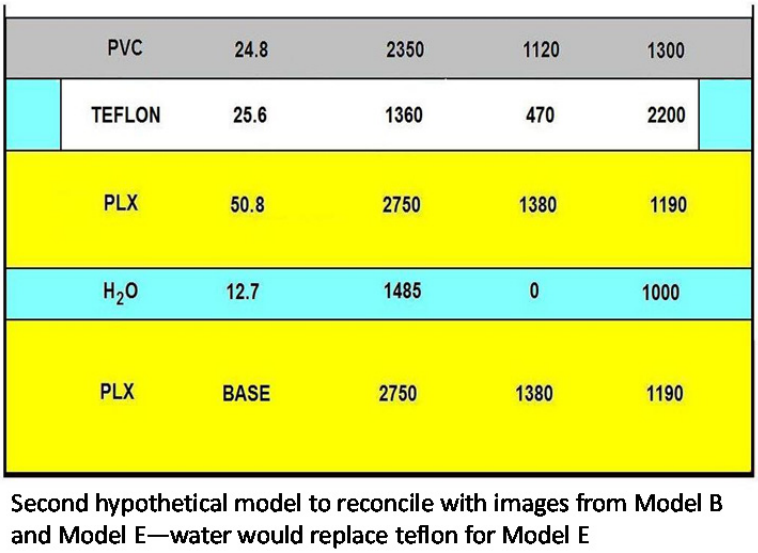

FIG. 38. Candidate model No. 2—considered for compatibility with processed images for Model B and Model E—Model E obtained by replacing Teflon with continuous water layer. This model was also rejected, based on inconsistencies with the images.

Confronted by the Processor with rejection of the Figure 37 model, the Modeller then submitted the schematic shown in Figure 38, asserting once again that this was, in fact, the correct model, and that once again model B and model E differed only in the presence of the Teflon block in the second layer.

This model seemed initially more plausible, in light of the position of the removable Teflon block in the second layer. The surface multiples and energy attenuation observed in the model B data would be explained by the presence of this block, as would the slight reflection event timing disparities between the centre of model B and its edges, which are unaffected by the Teflon. Since Teflon is lossy compared with water, this explains the lower S/N of the model B images, except at the edges where the model is the same as model E.

However...when we introduced a marker scale indicating the zero-offset reflection times for the layer boundaries in the model in Figure 38, with the Teflon layer replaced by water, into the CMP stack for Model E in Figure 39, we found that only the first of four boundaries matches a significant event on the seismic response, and there are clearly more events on the CMP image than we can account for with the Figure 38 model, even including possible multiple reflections. Likewise, posting the same time marker scale on the CMP stack for model B shows a similar mismatch. At this point it was obvious that, while the shallow removable Teflon block in the Figure 38 model could explain some image differences between the CMP stacks for models B and E, the layering depicted could not explain the reflection events actually observed, either in timing or in number.

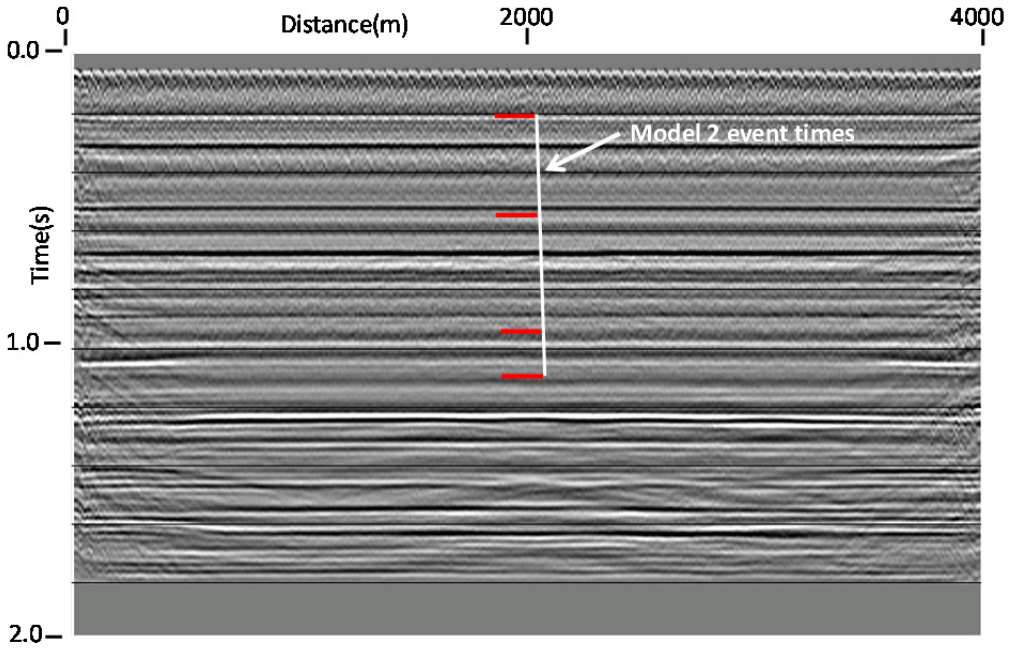

FIG. 39. This CMP stack of Model E shows the incompatibility with reflection event times computed from candidate model No. 2 that led to rejection of this model. Not only do none of the event times except the first tie with significant image reflections, but there are not enough reflecting interfaces in the model to generate deeper reflections seen in the image.

Finally, the Modeller confessed that he had yet again 'mistakenly' given the wrong model diagram to the Processor and offered yet another candidate for consideration, depicted in Figure 40. Candidate model no. 3 is nearly the same as candidate model no. 1, except for the placement of the removable Teflon block. We constructed a reflection time scale from this model and superimposed it on the CMP stack for either model E or the

edges of model B. Now there was a close match between layer boundary reflection times and actual events on the CMP stacks (Figures 41 and 42). The Processor was finally able to confirm that Figure 40 likely depicts the correct model.

1	PVC		25.4mm	2350	1120	1300	
2	WATER	TEFLON	6.7mm	1360	470	2200	WATER
3	PLX		50.8mm	2750	1380	1190	
4	PHN		66.9mm	3500	1700	1350	
5	PLX		25.4mm	2750	1380	1190	
6	WATER		12.7mm	1485	0	1000	
7	PLX		25.4mm	2750	1380	1190	

Third hypothetical model to reconcile with images from Model B and Model E—water would replace teflon for Model E

FIG. 40. Candidatel model No. 3—considered for compatibility with processed images for Model B and Model E—Model E obtained by replacing Teflon with continuous water layer. This model is consistent with all features seen on images for both Model B and Model E.

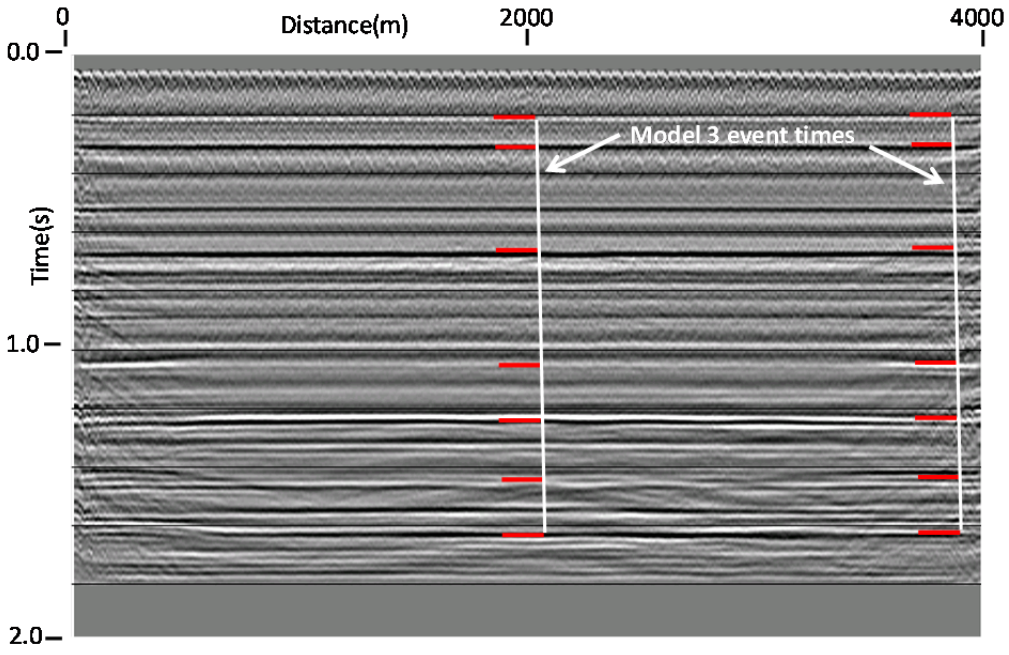

FIG. 41. CMP stack of Model E vs. reflection event times computed from the parameters of model No. 3, which closely match prominent events on the image, except for possible inter-bed multiples, which we have not attempted to remove. The tie is actually better at the edges of the image, especially for the 1050ms event, indicating the need to improve NMO for that event.

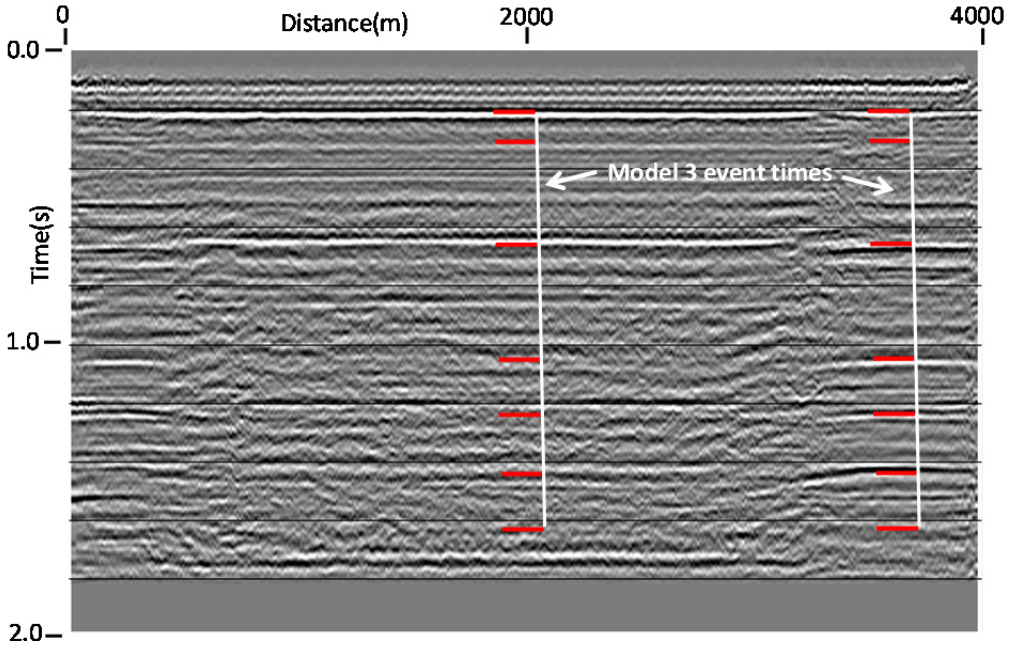

FIG. 42. The match of event reflection times from model No. 3 with the image from Model B. The match is good at the edge, still reasonable in the centre, although NMO velocities there should be modified to reflect the presence of the shallow Teflon layer.

CONCLUSIONS

We consider this exercise a very worthwhile validation not only of physical modeling and its usefulness, but of analytic processing. Physical modeling allows us to carefully control the elastic wave environment, so that we can usually identify, with some degree of certainty, the origin of each event visible on seismic records obtained by surveying the model. Analytic processing allows us to take these seismic records and not only estimate various physical parameters of the model, but to identify problems with the model itself, or difficulties with the surveying process and correct them. In this study, for example, the reflecting interfaces all appeared initially to have a slight dip, which may have been due to a slight variation of thickness of the shallowest layer, or to a persistent source coordinate error; and this effect was removed with a simple trace header modification. As we have shown in this particular study, a physical model can manifest an undesirable effect—in this case, surface-related multiples—which can be used to design and refine a processing stream to deal specifically with the effect.

Finally, this study has shown that with almost no knowledge of the actual model, as is often the case in field seismic surveys, careful processing can lead to images which can rule out proposed models which are incorrect in some respects. This is, in effect, a validation of the seismic imaging process, at least insofar as physical modeling is concerned. A similar approach on field data can be used to limit the range of earth models which are consistent with the observed data.

ACKNOWLEDGEMENTS

The authors acknowledge CREWES and its sponsoring companies for financial support, as well as NSERC for matching funding.

REFERENCES

Henley, D.C. 2003, Coherent noise attenuation in the radial trace domain, Geophysics, **68**, No. 4, pp1408-1416.

Henley, D.C., 2011, Now you see it, now you don't: radial trace filtering tutorial, CREWES research report—Volume 23(2011).

Henley, D.C., 2008, Raypath interferometry: statics in difficult places, 78th Annual international meeting, SEG, Expanded abstracts, 1263-1267.

Henley, D.C., 2010, Hybrid raypath interferometry: correcting converted wave receiver statics, 80th Annual international meeting, SEG, Expanded abstracts, 1861-1865.

Henley, D.C., 2012, Interferometric application of static corrections, Geophysics, 77, No. 1, Q1-Q13.

Henley, D.C., Raypath interferometry for dummies: a processing guide, CREWES research report Volume 20(2010)

Taner, M. T., 1980, Long-period sea-floor multiples and their suppression, Geophysical Prospecting, **28**, No.1, pp30-48.

Wong, J., Mahmoudian, F., Gallant, E., and Bertram, M., Seismic physical modeling measurements on solid surfaces, CREWES research report—Volume 22(2010).

Wong, J., Mahmoudian, F., Gallant, E., and Margrave, G.F., Physical modelling III: acquiring modeled data for VVAZ/AVAZ analysis, CREWES research report—Volume 23(2011).